Characteristics and Variability of Precipitation Across Different Sectors of an Extra-Tropical Cyclone: A Case Study Over the High-Latitudes of the Southern Ocean

S C H Truong, S T Siems, P T May, Y Huang, Étienne Vignon, A Gevorgyan

JGR Atmospheres

RESEARCH ARTICLE
10.1029/2023JD039013

Special Section:
Southern Ocean clouds, aerosols, precipitation and radiation

Characteristics and Variability of Precipitation Across Different Sectors of an Extra-Tropical Cyclone: A Case Study Over the High-Latitudes of the Southern Ocean

S. C. H. Truong[1,2], S. T. Siems[2,3], P. T. May[2], Y. Huang[4,5], É. Vignon[6], and A. Gevorgyan[2,7]

[1]Climate Science Centre, CSIRO, Aspendale, Victoria, Australia, [2]Monash University, Melbourne, Victoria, Australia, [3]ARC Securing Antarctica's Environmental Future, Melbourne, Victoria, Australia, [4]The University of Melbourne, Melbourne, Victoria, Australia, [5]ARC Centre of Excellence for Climate Extremes, Melbourne, Victoria, Australia, [6]Laboratoire de Météorologie Dynamique-IPSL, Sorbonne Université/CNRS/École Normale Supérieure-PSL Université/École Polytechnique-Institut Polytechnique de Paris, Paris, France, [7]Climate Service Division, Hydrometeorology and Monitoring Center, Yerevan, Armenia

Abstract Shipborne observations from the CAPRICORN-2018 field campaign were used to investigate the characteristics and variability of precipitation across different sectors of an extra-tropical cyclone on 16 February 2018, over the Southern Ocean (SO). Three distinct time periods—frontal, post-frontal, and cyclone—were identified during the day. The frontal passage recorded a total accumulation of 1.9 mm, where the precipitation phases were primarily composed of rain (96%), while the cyclone period recorded the largest precipitation (4.0 mm), where the precipitation phases varied with snow (10%), mixed-phase (40%), and rain (50%). The BASTA radar suggests the freezing level was shallow (~500 m) with snow present above. The cloud top heights, observed by a C-band radar, were shallower in the cyclone period, although deeper cloud depths of ~6 km were sporadically recorded. Increased surface fluxes and a southerly wind direction indicate that cold air advection, was likely the main cause of high precipitation during the cyclone period. A non-precipitating multi-layer cloud structure with a geometrically thin (200 m) homogeneous layer of supercooled liquid water (SLW) overlaying shallow boundary layer convection was seen during the post-frontal period. The ship-borne observations were used to evaluate Weather Research & Forecasting (WRF) simulations with different microphysics settings. We found the frontal precipitation intensity is well reproduced, but it is underestimated during the cyclone period. This study represents a unique set of observations and highlights the need for understanding how ice processes and potentially horizontal advection contribute to the development of precipitation and convection over the SO.

Plain Language Summary There are still significant differences between current precipitation products over the Southern Ocean (SO). This makes it harder to understand the hydrological cycle and different meteorological processes in the region. In this study, we used the shipborne observations from the **C**louds, **A**erosols, **P**recipitation, **R**adiation, and atmospher**I**c **C**omposition **O**ver the southe**R**n ocea**N** (CAPRICORN) 2018 field campaign to investigate the characteristics and variability of precipitation across different sectors of an extra-tropical cyclone on 16 February 2018, over the SO. Overall, the frontal passage recorded a total accumulation of 1.9 mm, with 96% of its phases being rain, while the cyclone period recorded the highest precipitation (4.0 mm), with 10% being snow and 40% being mixed. In addition, we made use of the observations to evaluate simulations run with the Weather Research and Forecasting Model (WRF) using a variety of cloud microphysics parameters. We observed that the intensity of the precipitation along the front is reproduced quite well, but that it is significantly underestimated throughout the cyclone period. This work highlights the importance of knowing the role that ice processes and potentially horizontal advection play in the formation of precipitation over the high latitudes of the SO.

Key Points:

- Distinctive characteristics of precipitation across different sectors of an extra-tropical cyclone are observed
- Largest precipitation was recorded during the cyclone period where its phases were largely constituted of mixed-phase and snow
- WRF reproduced the frontal precipitation intensity, while it is underestimated during the cyclone period

Supporting Information:

Supporting Information may be found in the online version of this article.

Correspondence to:

S. C. H. Truong,
son.truong@monash.edu

Citation:

Truong, S. C. H., Siems, S. T., May, P. T., Huang, Y., Vignon, É., & Gevorgyan, A. (2023). Characteristics and variability of precipitation across different sectors of an extra-tropical cyclone: A case study over the high-latitudes of the Southern Ocean. *Journal of Geophysical Research: Atmospheres*, *128*, e2023JD039013. https://doi.org/10.1029/2023JD039013

Received 6 APR 2023
Accepted 3 NOV 2023

1. Introduction

Large differences continue to exist in the amount, frequency and thermodynamic phase between various precipitation products over the high latitudes of the Southern Ocean (SO) (poleward of the Antarctic polar front) (Behrangi et al., 2016; Behrangi & Song, 2020; Boisvert et al., 2020; Manton et al., 2020). Fundamentally these differences arise from a lack of high-quality observations suitable for evaluation across a range of temporal and spatial scales. Observations from isolated island sites are often intermittent and can suffer from orographic effects

(Manton et al., 2020), and sparse ship observations are often of limited quality due to limited instrumentation, the harsh physical environment and sampling biases (Siems et al., 2022).

While numerous precipitation products have been evaluated against surface observations from Macquarie Island (Lang et al., 2020; Tansey et al., 2022; Wang et al., 2015), this site is located at 54.5°S, amid the SO storm track rather than at high latitudes. Both satellite observations (Mace et al., 2009) and recent field observations (Montoya Duque et al., 2022; Truong et al., 2020, 2022) have identified the unique nature of the thermodynamics and cloud structure across the lower free troposphere and boundary layer at these high latitudes. Mace et al. (2009) used active remote sensing from the A-train satellites to note that this region has the highest frequency of low and mid-level clouds across the globe, even in comparison with comparable latitudes of the North Pacific and North Atlantic.

Beyond the complex cloud macrophysics, the cloud microphysics and dynamics also challenge our ability to develop robust precipitation products for these latitudes. The pristine SO has been observed to have relatively few ice nuclei (McCluskey et al., 2018) with supercooled liquid water (SLW) and mixed phase clouds are found to be more prevalent than comparable clouds over the North Pacific and North Atlantic (Hu et al., 2010; Huang et al., 2012; Mace et al., 2021; Morrison et al., 2011). These clouds often exist at temperatures colder than that of the Hallett-Mossop process (−8 to −3°C), suggesting that relatively poorly understood secondary ice production processes (Järvinen et al., 2022; Korolev & Leisner, 2020; Sotiropoulou et al., 2020) can be involved in the production of precipitation. Further a variety of dynamical mechanisms are known to exist at these latitudes including polar vortices and meso-vortices, fronts, and atmospheric rivers, but have rarely been studied (Gordon et al., 2023; McCoy et al., 2021; Rauber et al., 2020).

Ye et al. (2014) noted the importance of developing a better understanding of the physical processes that govern cloud formation and precipitation in order to reduce uncertainty in precipitation estimates over the high latitudes. Accordingly, several studies have employed the recent field observations (McFarquhar et al., 2021; Sellegri et al., 2023) to define case studies over the SO in an effort to identify these key dynamical and microphysical processes (Atlas et al., 2020; Lang et al., 2021; Lasher-Trapp et al., 2021; Vignon et al., 2021). These efforts have all employed numerical simulations, enabling sensitivity studies, especially of microphysical processes. Over the lower latitudes of the SO (between the subtropical ridge and the SO storm track), mixed phase clouds have also been found to be critical in the development of precipitation, particularly within open mesoscale cellular convection (Ahn et al., 2017; Lang et al., 2021, 2022) where the Hallett-Mossop rime splintering process was first encountered (Huang et al., 2021; Mossop, 1970). Along the coast of Antarctica, Vignon et al. (2021) studied the thermodynamic phase of mid-level clouds (cloud tops of 5–6 km) during the passage of a warm front, noting the sensitivity of the phase to the microphysics parameterization scheme.

Motivated by the need to better understand the dynamics and microphysics of clouds and precipitation events at the high latitudes of the Southern Ocean, we examine a case study first introduced in Truong et al. (2020, their Figure 7) that focused on the cloud transitions across an extra-tropical cyclone located poleward of the polar ocean front. This case study featured the second largest precipitation "day" (0–24 UTC, 16 Feb 2018) observed by the research vessel (RV) Investigator during the CAPRICORN 2018 (**C**louds, **A**erosols, **P**recipitation, **R**adiation, and atmospher**I**c **C**omposition **O**ver the southe**R**n ocea**N**) campaign as observed by an OceanRain disdrometer (Klepp et al., 2018). Our study of precipitation is further enriched with observations from a scanning C-band dual-polarization Doppler radar (OceanPOL) on-board the RV Investigator. We note this case study nearly coincides in time with that of Vignon et al. (2021) (Feb 14–16, 2018), centered some 3540 km away to the southeast. The case study is of further interest as there was found to be only limited consistency between the fifth generation European Center for Medium-Range Weather Forecasts Re-Analysis (ERA5) precipitation, the Integrated Multi-satellitE Retrievals for the Global Precipitation Measurement [GPM (IMERG)] (Huffman et al., 2019) and the surface observations from the RV Investigator (Figure 1). Our objectives are two-fold: first, we investigate the synoptic meteorology and characteristics of a relatively heavy precipitation event across different sectors of an extra-tropical cyclone located poleward of the ocean polar front, which includes a ∼6-hr period of multi-layer clouds. The ship observations are used to evaluate ERA5 and GPM (IMERG) precipitation at the event scale. Second, we employ numerical simulations to further define the dynamics and precipitation processes encountered, as evaluated against the field observations. Going further, we test the sensitivity of precipitation in these simulations to different microphysics parameterizations. This comprehensive case study allows us to understand the role of high latitude, extra-tropical cyclones in contributing to surface precipitation and free troposphere cloud cover and to examine their representation in convection-permitting models.

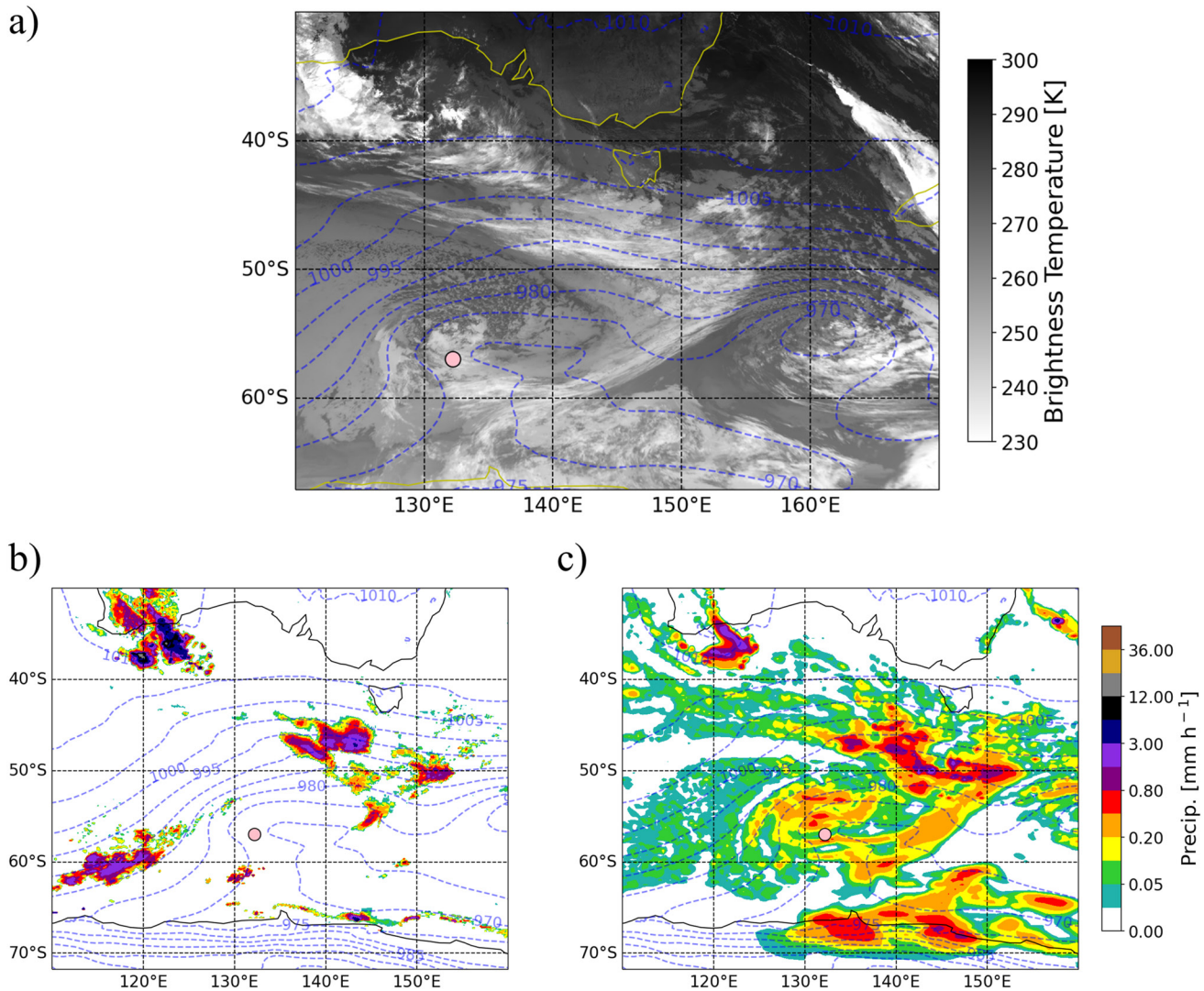

Figure 1. A snapshot of the cloud cover and surface precipitation over the Southern Ocean on 16 Feb 2018 at 18 UTC. (a) Himawari 8 brightness temperature (channel 14) with the ship location indicated as a pink dot and an overlay of the mean sea level pressure (hPa) (blue dashed line) (b) the estimated precipitation from the GPM (IMERG), Level-3 product. (c) The diagnosed precipitation from the ERA5 reanalysis. The blue dashed lines in (b) and (c) are as in (a).

2. Data

2.1. Shipborne Observations

The 2018 CAPRICORN voyage took place aboard the Australian Marine National Facility (MNF) RV *Investigator* from 11 Jan to 21 Feb 2018, traversing the SO from south of Tasmania, covering an area of 43°S–65°S (Figure 1, Truong et al. (2020)). A detailed summary of the observational data during the 2018 CAPRICORN is provided in McFarquhar et al. (2021). We provided a short description of the equipment used in this study including: a cloud radar (the Bistatic Radar System for Atmospheric Studies: BASTA), a weather radar (OceanPOL), a cloud lidar [Bureau of Meteorology (BoM) lidar] and an OceanRain (ODM) in the supplementary document (Table S1 in Supporting Information S1).

2.2. Satellite Observations

High-resolution Himawari-8 cloud products (Heidinger, 2011; Pavolonis, 2010) provided by the BoM are also used, including the cloud-top temperature (CTT), cloud-top pressure (CTP) and cloud-top phase (CTPs) retrievals. These cloud products are generated by the BoM using the GOES-R Advanced Baseline Imager Cloud Height

Algorithm (ACHA) (Heidinger, 2011). The data is retrieved at a spatial and temporal resolution of 2 km and 10 min, respectively.

The Global Precipitation Measurement (GPM) provides three different levels of data products which can be retrieved from the NASA website. This study focuses on the GPM (IMERG) Level 3 product ($0.1° \times 0.1°$ spatial resolution between 60°S and 60°N). We used a multi-satellite precipitation estimate with gauge calibration (mm h^{-1}) in this study. More detailed information and an algorithm description can be found at Huffman et al. (2019).

2.3. Reanalysis Data

The ERA5 reanalysis (Hersbach et al., 2023), produced by the European Center for Medium-Range Weather Forecasts (ECMWF), is based on the global Numerical Weather Prediction (NWP) model Integrated Forecast System (IFS) version CY41R2 (Hersbach et al., 2020). The model provides hourly estimates of atmospheric variables, at a horizontal resolution of 31 km and 137 vertical levels from the surface to 0.01 hPa. The data is available at both surface (e.g., total precipitation) and 37 pressure levels (e.g., vertical winds).

2.4. Weather Research & Forecasting Model Configuration

The Weather Research & Forecasting Model (WRF, version 4.2.0) is based on non-hydrostatic Euler equations, designed for both mesoscale atmospheric research and operational forecasting (Skamarock et al., 2019). In this study, the model is configured with a parent domain and two one-way nested domains which downscales the model horizontal resolutions from 9 to 1 km (3:1 ratio, Figure 2g). The simulation from the innermost domain (1 km resolution) is used for analysis unless stated otherwise. The WRF simulations apply 96 terrain-following eta levels with 60 levels located in the lowest 3 km AGL. The outer domain covers a broad area of the SO between 44° and 66°S and 100°E and 160°E, whereas the nested domains were configured to capture the ship track during the simulation period. The ERA5 reanalysis, produced by ECMWF provide the initial and lateral boundary conditions for all experiments hourly at ∼30 km horizontal resolution and 37 pressure levels. The simulation is initialized at 0 UTC 15 Feb. 2018, and runs for a period of 48 hr. A 24-hr spin-up period is used to stabilize the model. For the control simulation (Ctrl-96), the configuration is analogous to previous WRF simulations over the SO as in Lang et al. (2021) except for the microphysics scheme and the number of vertical levels (e.g., 96 level). The Yonsei University (YSU) PBL scheme (Hong et al., 2006) was used. The Simplified Arakawa-Schubert (SAS) cumulus scheme (Pan & Wu, 1995) was employed for the 9-km parent resolution domain, while the convective parameterization option for the two nested domains was turned off. The Noah-MP (multi-physics) Land Surface Model (Niu et al., 2011) is used. Finally, the shortwave and longwave radiation processes follow the Rapid Radiative Transfer Model for GCMs (RRTMG) shortwave and longwave radiation scheme (Iacono et al., 2008; Mlawer et al., 1997). For the control simulation (Ctrl-96), the Morrison semi-double-moment bulk microphysics scheme (Morrison et al., 2005) is used. The scheme has a single-moment (prognostic mass concentration only) treatment of cloud droplets and a double-moment (prognostic mass and number concentrations) treatment of cloud ice, rain drops, snow, and graupel particles. The cloud condensation nuclei (CCN) is set to 100 cm^{-3} (Lang et al., 2021; Vignon et al., 2021).

Due to the complexity of ice processes, bulk parameterization of cloud microphysics is particularly challenging. Vignon et al. (2021) reported that the default version of the Morrison microphysics scheme (Morrison et al., 2005, 2009) produced almost fully glaciated clouds and further highlighted that the replacement of three existing heterogeneous ice nucleation mechanisms, including contact freezing (Meyers et al., 1992), deposition/condensation freezing (Cooper, 1986), and immersion freezing (Bigg, 1953), by an empirical parameterization based on measurements at Mawson station helped to reduce the ice production rate, largely due to immersion freezing, at the cloud tops. The detailed INPs parameterization scheme is provided in Vignon et al. (2021), Section 2.1.1, which we employ in a sensitivity study. We present two simulations (Table 1) to investigate the impact of the representation of microphysical processes (MP1) on the simulations.

2.5. Cloud Resolving Model Radar Simulator (CR-SIM)

To provide a comparison of the C-band radar observation to the WRF simulation, the Cloud Resolving Model Radar Simulator [CR-SIM, Oue et al. (2020)] version 3.32 has been used. CR-SIM uses the T-matrix method

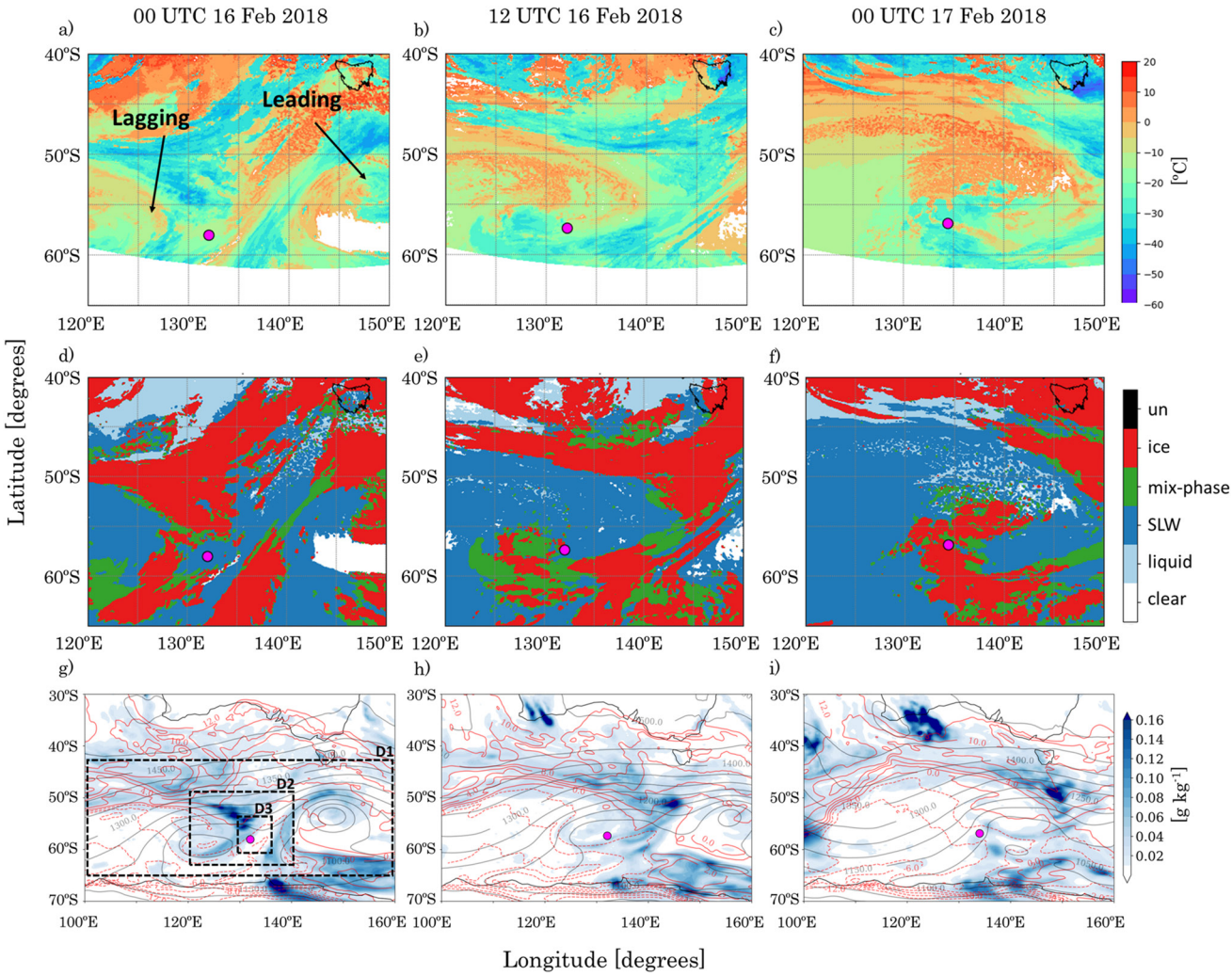

Figure 2. Map of synoptic conditions around the ship 00 UTC 16 Feb 2018 (first column), 12 UTC 16 Feb 2018 (middle column) and 00 UTC 17 Feb 2018 (last column). The magenta dot indicates the position of the RV Investigator at the corresponding times. (a–c) The Cloud top temperatures (CTTs) from Himawari-8 (°C). (d–f) The cloud top phase classification from Himawari-8 and (g–j) The 500 hPa geopotential height (black contours). The solid and dashed red contours present positive and negative 900 hPa temperatures in degrees. The color shading shows the vertically integrated condensed water content (ICWC, sum of cloud liquid droplets, cloud ice crystals, snow, and rain species; unit: g kg^{-1}). Data in g-j are from the ERA5 reanalysis. The three WRF simulation domains (D1, D2, and D3) are shown in (g). The leading and lagging cyclones are noted in (a).

developed by Mishchenko and Travis (1998) for computing the scattering properties of 6 different hydrometeors, including cloud water, cloud ice, rain, snow, graupel, and hail. In this study, CR-SIM has been configured as a virtual C-band dual-polarization Doppler radar at a frequency of 5.5 GHz. More information about CR-SIM can be found in Oue et al. (2020).

Table 1
Model Configuration

Experiment	PBL scheme	MP scheme	Vertical resolution	Modification
Ctrl-96	YSU	Morrison	96 η-levels	–
MP1	YSU	Morrison	96 η-levels	Low INPs

3. Synoptic Meteorology

We focus on a 24-hr period from 00 to 24 UTC 16 Feb (00 Feb 17) 2018, with particular emphasis on the last 6 hr when the precipitation was most intense. Figure 1a shows an overview of the synoptic conditions around the ship at 18 UTC on 16 Feb 2018. Notable differences between the estimated and diagnosed precipitation from the GPM (IMERG) and the ERA5 reanalysis is seen in Figures 1b and 1c, respectively.

This extra-tropical cyclone is relatively strong for these latitudes. Messmer and Simmonds (2021) found that ~20% of SO cyclones had a minimum central

pressure lower than 967 hPa. The cyclone originally formed off the west coast of Africa (35.0°E, 38°S) (Fig. S1a in Supporting Information S1) on 11 Feb 2018, reaching its minimum central pressure of 967 hPa at 18 UTC 16 Feb. The ship was close (~110 km around 12 UTC) to the extra-tropical cyclone center (132.0°E, 57.51°S) which has an intensity of 970.9 hPa. Figure 2 shows that, initially, at 00 UTC 16 Feb, the ship was located ahead of an advancing front (Figure 2a), between two mid-latitude cyclones. The leading cyclone was more intense at 954 hPa, while the trailing cyclone was at 973 hPa (Figure 2a) at this time. This front advances over the ship at about 09 UTC 16 Feb leaving the ship in a steady post-frontal region for approximately 6 hrs before it encounters the weaker trailing cyclone around 15 UTC 16 Feb, which had strengthened to 969.8 hPa. We break the analysis into three time periods: frontal (00–09 UTC), post-frontal (09–15 UTC) and cyclone (15–24 UTC) for 16 Feb 2018.

Properties of the cloud cover across the domain, such as the cloud-top temperatures (CTTs; Figure 2 row 1) and cloud-top phases (CTPs; Figure 2 row 2) from Himawari-8, rapidly change with the evolving synoptic meteorology. The eastward moving frontal cloud band with CTTs colder than −40°C can be observed at these times (Figures 2a–2c). The leading edge of the frontal band is seen to advance rapidly, roughly 10° latitude every 12 hr, passing over the ship at around 09 UTC. At the ship's location, the CTTs around the ship's location were approximately −20, −15, and −35°C at the sample times of Figures 2a–2c. The deep cloud of the trailing cyclone was present over the ship from 16 UTC 16 Feb until 08 UTC 17 Feb. After this time when the cyclone passed, the region was influenced by large open mesoscale cellular convective clouds (not shown). The Himawari-8 CTPs suggested the trailing cyclone (16–24 UTC Feb 16) were glaciated at cloud top. SLW was observed surrounding the ship location in the pre-frontal period (Figure 2d), and behind the frontal passage (Figure 2e).

The leading strong cyclone is followed by shallow post-frontal clouds to the southwest at 00 UTC 16 Feb, suggesting that a significant cold air outbreak (CAO) occurred (Fletcher et al., 2016a, 2016b). At 12 UTC the meteorology near the ship is defined by the trailing cyclone with a large region of relatively shallow/warm post-frontal clouds located to the north of the ship, extending well past the polar ocean front into the lower latitudes of the SO. These postfrontal clouds are composed of SLW at cloud top according to Himawari-8. At 00 UTC 17 Feb, this post-frontal cloud mass dominates much of the image to the north of the ship.

ERA5 estimates of vertically integrated ice water content (ICWC) show a relatively large amount formed along the extended frontal band that passed over the ship location. The ERA5 reanalysis produces little ICWC after the frontal passage, even when the extra-tropical cyclone passed over the ship. We further note that there is little indication of an atmospheric river [for example, vertically integrated horizontal water vapor transport (IVT)] feeding water into this high-latitude cyclone.

4. Observations

4.1. Surface Observations

We now examine the surface observations from R/V Investigator. The time series of observed surface temperature, relative humidity, wind speed, and wind direction (Figure 3) further demonstrates that the ship encountered two distinct transitions over the 24-hr period. At 08:30 UTC, the wind direction shifted rapidly from a heading of 20°–290°, while at 17:30 UTC the wind direction shifted from 215° to 145° and was accompanied by an increase in wind speed from 9 to 14 m s^{-1} (Figure 3b) corresponding to the passage of the front and the low-pressure system, respectively.

4.1.1. Frontal (00–09 UTC)

During this period the surface temperature was quite steady at 3°C while the relative humidity increased gradually from ~62% to ~96%. The wind speed increased from 6 to 10 m s^{-1} before dropping at 06 UTC. A weakening component of the wind during the frontal passage can be seen just after 06 UTC, corresponding to shifts in wind direction, wind speed and relative humidity. Surprisingly, the surface air temperature increased when the wind direction shifted across the front. Normally, a northerly pre-frontal air mass would lead to warm air advection ahead of the front (Zheng & Li, 2019), which would be followed by a colder post-frontal air mass. We attribute this to two conditions, first a significant cold air outbreak (CAO) event is associated with the strong leading front (954 hPa), and second, the high latitudes of the Southern Ocean are known for very weak SST gradients (Dong et al., 2006). Back trajectories taken across this front (Fig. S2 in Supporting Information S1) show that the northerly pre-frontal air mass (the CAO) originated at higher latitudes before reversing directions when the front arrives. Technically the ship encountered a warm front instead of a cold front. No significant changes were observed for the surface sensible (SHF) and latent heat

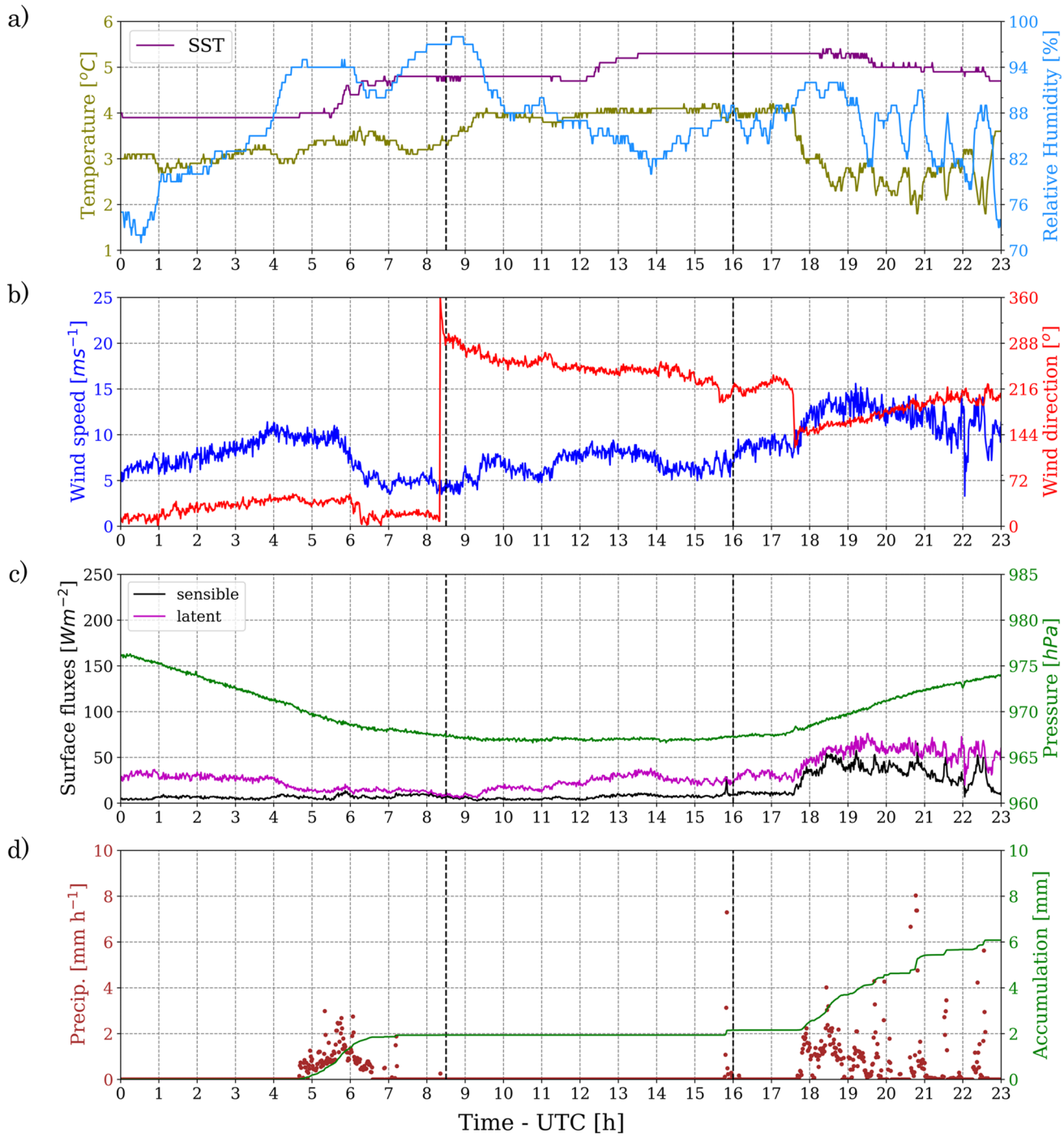

Figure 3. Time series of (a) temperature (°C), sea surface temperature (°C) and relative humidity (%), (b) 10 m wind speed (m s^{-1}) and 10 m wind direction (°), (c) latent and sensible heat fluxes (W m^{-2}) and pressure (hPa) and (d) surface precipitation (mm h^{-1}) and accumulated precipitation (mm) observed by ODM. Temporal resolution is 1 min for all panels. Vertical dashed black lines approximately separate the three meteorological events.

fluxes (LHF) across the frontal passage, although the SST increased by 1°C. Frontal precipitation (96% probability of rain) was detected by the ODM from 05 to 07 UTC with a peak rate of 3 mm hr^{-1} and a total accumulation of 1.9 mm.

4.1.2. Post-Frontal (09–15 UTC)

After the frontal band passed the ship, the surface air temperature increased by 1°C over an hour and then remained steady from 08:00 to 17:00 UTC, while the relative humidity dropped from 96% to 82%. Through this post-frontal

period, the winds are seen to steadily rotate from westerly (280°) to southwesterly (220°). These surface winds are primarily directed away from the approaching cyclone (Figures 2a and 3b). The ODM suggests no precipitation reached the ocean surface during this period. We also note continued weak surface fluxes through this stage of the event. Both the sensible and latent heat flux are well below 50 Wm^{-2}. Through the first 15 hr of this day, only weak latent heat fluxes are evident, limiting the supply of water vapor available for any precipitation.

4.1.3. Cyclone (15:00-24:00 UTC)

A second transition was observed with the arrival of the cyclone after 15 UTC. The surface air temperature dropped abruptly to below 3°C just before 18 UTC. After this time, surface latent heat fluxes more than doubled to about 60 Wm^{-2}, helping drive local convection. The sensible heat flux increased from 10 to 40 Wm^{-2}. The RH, temperature and winds are found to strongly fluctuate during this period of precipitation. While the wind direction changed from being southwesterly to more southerly, the wind speed also steadily increased to ∼15 m s^{-1}. The strongest precipitation of the study period was detected after 18 UTC with a peak rate of 8 mm hr^{-1} and a total accumulation of 4.1 mm over 7 hr in this stage. Both the intensity and duration were higher than during the frontal passage. The ODM suggests the probability of observed rain is reduced to 50% (10% of snow and 40% of mixed-phase) during the cyclone period (Fig. S6 in Supporting Information S1). The strong surface fluxes and the wind direction suggest that the precipitation in the cyclone was being driven by cold air advection, presumably from Antarctica, rather than warm air advection from an atmospheric river, consistent with a collection of HYSPLIT back trajectories (Figure S2 in Supporting Information S1).

4.2. Surface-Based Remote Sensing

4.2.1. Frontal (00–09 UTC)

During the frontal passage, the freezing level (i.e., ∼0°C) was shallow at around 500 m, where a sharp transition from 0.5 to larger than 3 ms^{-1} is evident in the Doppler vertical velocity observed with the BASTA cloud radar (Figure 4a). A change in the reflectivity (Figure 4a) was also seen below the freezing level (e.g., temperature larger than 0°C) from 04:30 to 07:30 UTC. The BASTA Doppler vertical velocity suggests snow above the freezing level during the frontal passage period (<1 m s^{-1}), and rain below the freezing level (>3 m s^{-1}). An abrupt change of vertical velocities near the surface and high reflectivity correlated well with the onset of precipitation as observed by the ODM (Figure 3d). The CTHs during the frontal passage were shallower (∼4 km) than those of the cyclone period (∼5.5 km). The observed CTHs from BASTA radar may be a slight underestimate due to attenuation, but roughly agree with the estimated depth (e.g., topmost saturation layer) from the upper air soundings at 04 UTC [500 hPa] (Figures 4 and 8). The cloud merged products suggest ice or mixed-phase clouds during the frontal passage. The passage of the front fully attenuated the lidar backscatter signal above the freezing level from 04 to 07 UTC (Figure 4d). The higher noise level is evident in the upper troposphere during the first 10 hr, which restricts the recoverable upper-level cloud information from lidar observation.

Moving to the C-band radar observation, the peak of the frontal cloud band was located to the northeast of the ship with a reflectivity greater than 30 dBZ (Figure 5a). The observed CTHs were approximately 6.5 km (Figure 5d) which is higher than the observed BASTA radar (4 km). The shallower CTHs in BASTA radar could be likely due to the attenuation of the BASTA signal. As the frontal cloud band progressed eastward, high reflectivity was generally observed within 50–100 km to the northeast of the ship location until 12 UTC. Smaller reflectivity within 50 km of the ship location was noticed during the frontal passage (Figure 5a).

A Contoured Frequency by Altitude Diagram (CFAD) for the C-band radar is constructed with a height sampling of 250 m (Figure 7a). The CFAD was calculated up to 7 km above ground level (AGL) corresponding to the vertical range of the CTH observations. During the frontal passage, the radar reflectivity increased toward low altitudes (20 dBZ). A similar increasing pattern is also seen in the histogram of ZDR with height (Fig. S4 in Supporting Information S1). Further investigating the plan position indicator (PPI) (Fig. S3a-S3c in Supporting Information S1) with two vertical cross-sections at 60° and 80° through the convective front, it could be due to ice/snow aggregation as the radar beam angle scanned at lower altitude, the higher reflectivity is observed. No evidence of a melting layer is resolved because of the low freezing level (500 m, Figure 7a).

4.2.2. Post-Frontal

The time series of the cloud phase by a radar-lidar merged product (Figure 4c) shows that multi-layer thin clouds, most of which primarily resided in the lowest 2.5 km, were detected from 09 to 16 UTC and mainly composed of SLW.

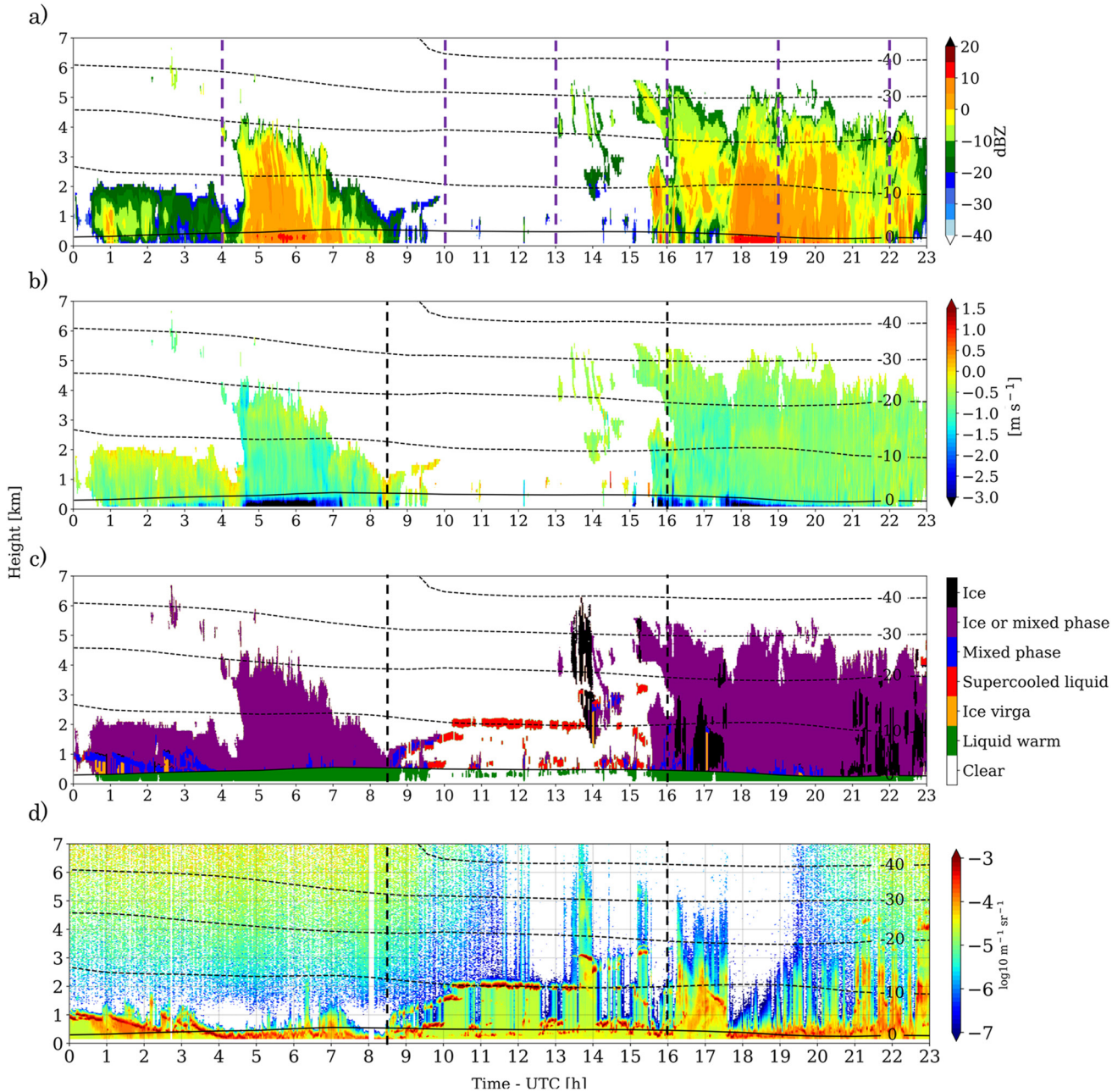

Figure 4. Time height plots of (a) the 95 GHz radar reflectivity dBZ from BASTA, (b) Doppler velocity ($V_{Doppler}$), (c) Cloud phase from the merged cloud radar and lidar and (d) cross-section of lidar attenuated backscatter aboard the RV Investigator on 16 Feb 2018. Dashed black contours indicate the air temperature from ERA5 (10°C intervals). Vertical dashed purple in (a) and black lines in (b)–(d) indicate the sounding launch times and the approximate time of the three meteorological events, respectively.

Visual inspection of the Himawari 8 cloud type (www.eorc.jaxa.jp) confirmed that the cloud field was characterized by scattered stratus and cumulus in the lowest kilometer. This period is also seen to be largely free of any precipitation.

4.2.3. High-Latitude Cyclone

Returning to the cyclone period again, a low-moderate reflectivity observed by the BASTA (>10 dBZ) was seen below the freezing level from 15:30 to 21 UTC (Figure 4a). The freezing level was again shallow at around 500 m. Analogous to the frontal period, there was also a sharp change in Doppler vertical velocity at the freezing level (Figure 4b) where the BASTA doppler vertical velocity suggests snow above the freezing level and both rain and snow below. As before, the abrupt change of vertical velocities and high reflectivity is well correlated with

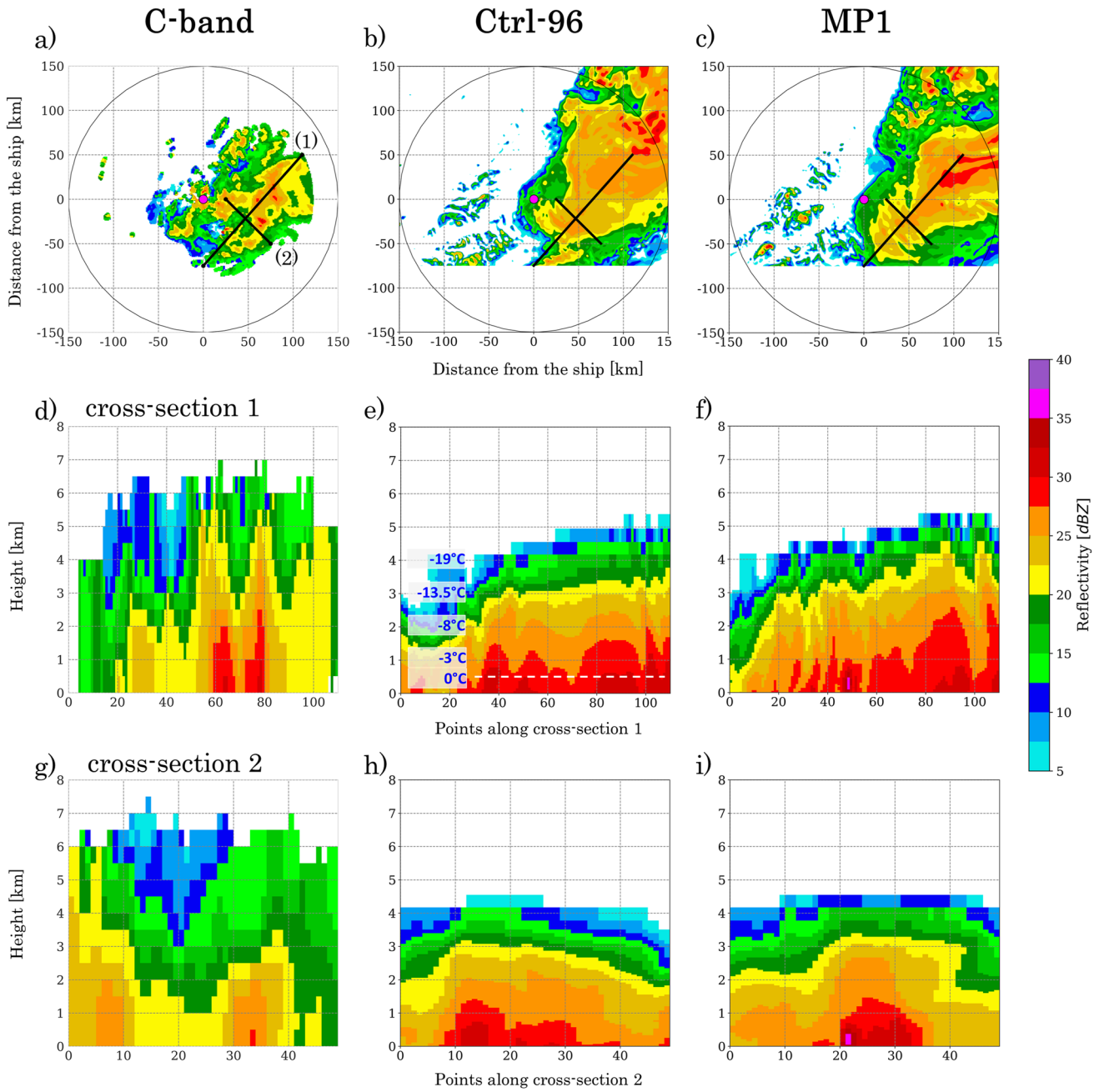

Figure 5. The observed (a) spatial C-band radar reflectivity from OceanPOL and WRF (b) Ctrl-96 and (c) MP1 reflectivity at 2 km AGL at 06 UTC 16 Feb 2018. The labels (1) and (2) associated with the black lines in panels a–c indicate the cross-sections which are plotted in d–f and g–i, respectively. Reference temperatures at different levels (0.5, 1, 2, 3, and 4 km) are shown in panel (e) Horizontal white dashed line indicates freezing level. The magenta dot indicates the position of the RV Investigator.

the precipitation as observed by the ODM (Figure 3d). The cloud merged product suggests ice or mixed-phase clouds during this time with the lidar backscattered signal fully attenuated at the freezing level (Figure 4d).

The cross sections of the C-band radar observations suggest that the cloud top altitude of the nearby cloud field is ~6 km (Figure 6d). The spatial coverage of the C-band radar differs between the frontal and cyclone periods with the convection being spread out across the domain but was patchier for the cyclone period. It is interesting to contrast the CFAD diagrams between the two periods. The radar reflectivity has a wider range (10–30 dBz) during the cyclone period from the surface up to 5 km (Figure 7d). This broader spectrum suggests a mixture of

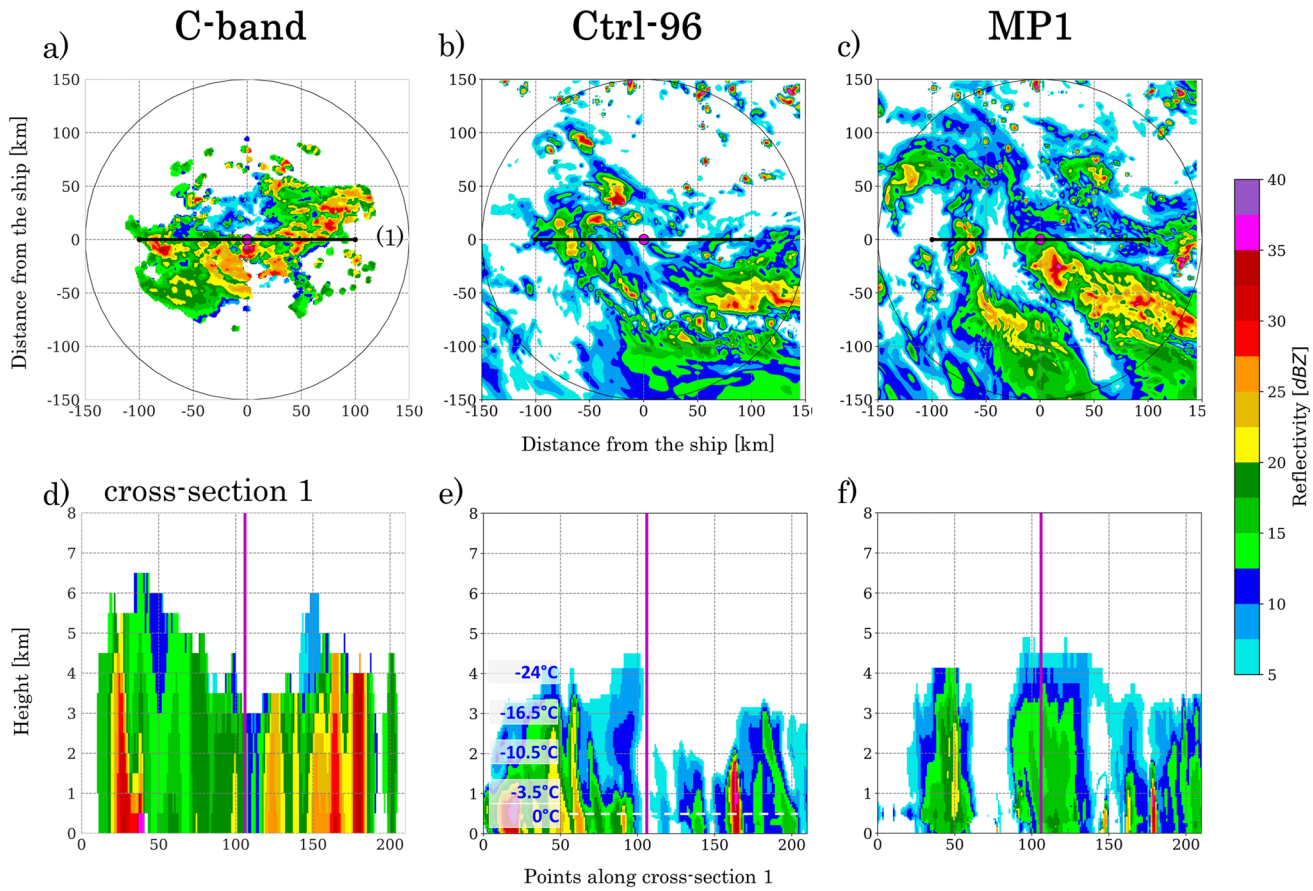

Figure 6. As for Figure 5 but at 18 UTC 16 Feb 2018, except the vertical purple line which indicates the ship location (purple dots in a–c) on the cross-sections.

hydrometeors and/or a wider size distribution being observed during the cyclone period. The higher frequency seen between 2 and 3 km during the cyclone period (Figure 7d) could, in part, be due to the patchy convection present across the domain. A vertical cross-section of the PPI (Fig. S3d-S3f in Supporting Information S1) suggests ice/snow aggregation is dominant during this time. Based on the sounding (Figures 8e and 8f), we speculate the southerly dry air contributes to melting the ice/snow in the low-level (<1.5 km), which could be another reason for lower frequency of high reflectivity toward the surface.

Overall, the C-band observation suggests the large presence of snow in deep clouds of both the frontal and cyclone periods. Using the reflectivity from the C-band radar as a proxy for highly convective regions, we calculated the mean reflectivity at 1 km above sea level (ASL) and within a radius of 5–10 km from the ship location (Fig. S5 in Supporting Information S1). High mean reflectivity coincides well with the peaks in ODM observation (Figure 3d).

4.3. Soundings

We finally examine the thermodynamic structure across the extra-tropical cyclone using the upper air soundings. During the frontal period (04 UTC, Figure 8a), the profile has relatively strong winds from the northwest from 500 to below 750 hPa, at which pressure it rotates to northeast in the boundary layer. The atmosphere is completely moist with the main inversion evident at 720 hPa (Figure 8a).

After the frontal band passed the ship, the profile (10 UTC; Figure 8b) suggests there are four layers of saturation where clouds could potentially be present (thin layers at 930, 880, 790, and 740 hPa). The main inversion was identified at 740 hPa, collocated with the uppermost cloud layer at that time (Figure 4c). A weak wind speed with shifting wind direction was recorded at different levels (Figure 8b). Similar to 10 UTC, mid-level (740–770 hPa) shear is evident at 13 UTC (Figure 8c), corresponding to the cloud layer, which suggests the importance of

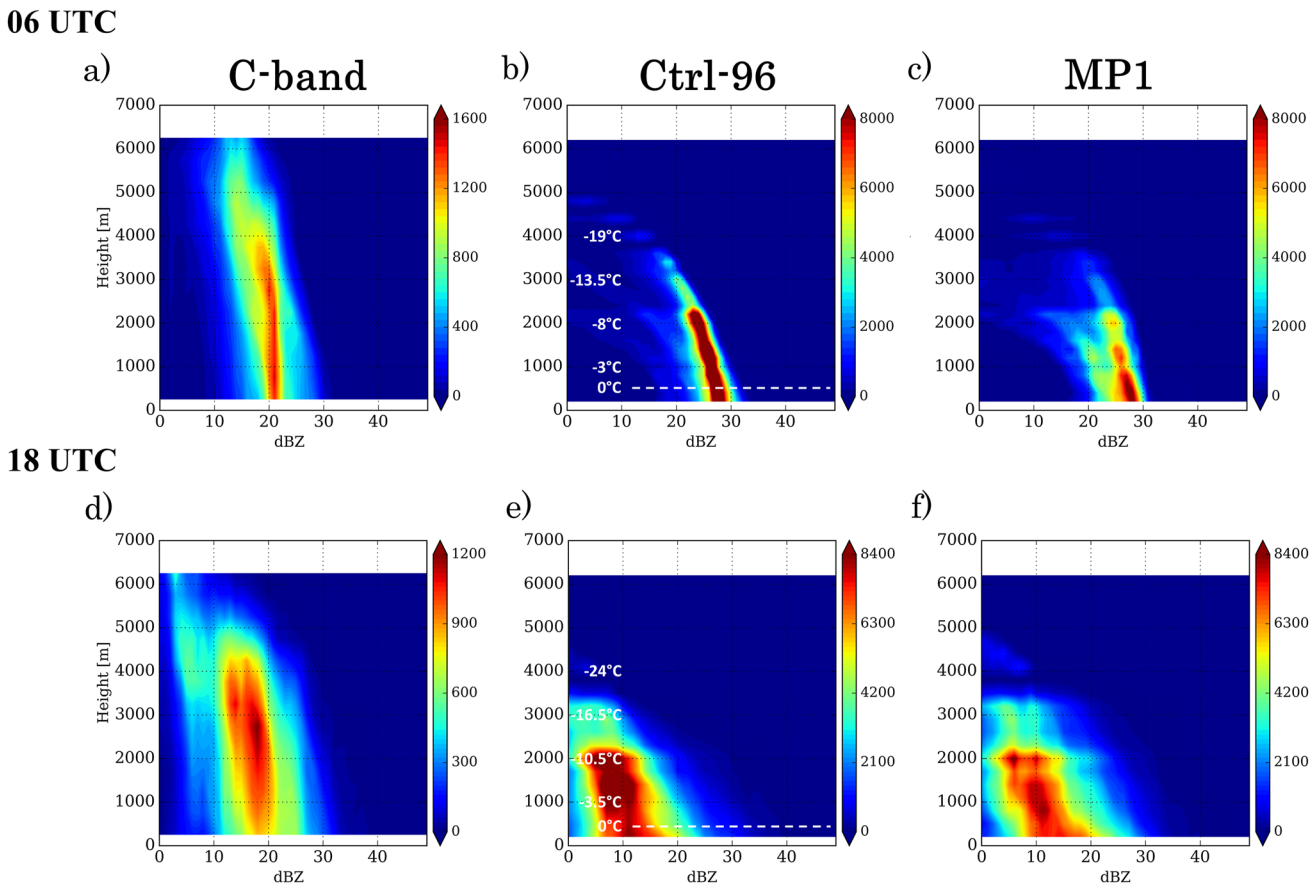

Figure 7. Contoured frequency with altitude (CFAD) diagrams for the observed (a) radar reflectivity (C-band) and WRF (b) Ctrl-96, and (c) MP1 reflectivity. The timing of the CFAD is 1 hr and at 06 UTC and 18 UTC for panels a–c and d–e, respectively. Reference temperatures at different levels are shown in panel (b) Horizontal white dashed line indicates freezing level obtained from the WRF simulation.

horizontal advection/shear in the formation of the thin cloud layer at 2.3 km altitude. Three distinct air masses are evident through the profile (surface to 830, 740–770, and above 650 hPa).

The following sounding (16 UTC; Figure 8d) at the start of the cyclone period, has greater moisture up to 650 hPa, consistent with the presence of clouds near the high latitude cyclone (Figure 4a). During the cyclone period (Figures 8e and 8f), southerly winds are observed. Virtually, no inversion is evident, and there is a high relative humidity up to 650 hPa, consistent with the convective clouds observed by the radars.

4.4. ERA5 and GPM (IMERG) Precipitation

Motivated by Figures 1b and 1c where the GPM (IMERG) spatially indicates there is no precipitation around the ship, we constructed a time series of GPM (IMERG) and ERA5 precipitation based on the nearest grid point to the ship location. Consistent with Figure 1b, no precipitation was recorded in the GPM (IMERG) product after the frontal passage (Figure 9). We further examined the Infrared (IR) Kalman filter weight that was used to produce the GPM (IMERG) precipitation to find out the potential causes of the GPM (IMERG) failure. During this period either the morphing-only or PMW-only (Passive Microwave) technique was being used (i.e., the Kalman filter's flag is equal 0). Montoya Duque et al. (2023), further use variables: "IRprecipitation" and "HQprecipitation" (PMW precipitation is defined as High-Quality, HQ, precipitation, Huffman et al. (2019)) to deduce whether the rain gauge calibrated precipitation rate estimates (precipCal) use the morphing-only or the PMW-only information. However, since the GPM (IMERG) does not show any precipitation in the cyclone period (Figures 1b and 9a and 9b), it was not possible to track whether morphing-only or PMW-only is being used. Regardless, both methods of precipitation estimation have disadvantages over the SO. First, the morphing-only estimate is limited by the temporal and spatial resolution since it is based on the MERRA-2 reanalysis (1 hr, 2.5°) for computing the

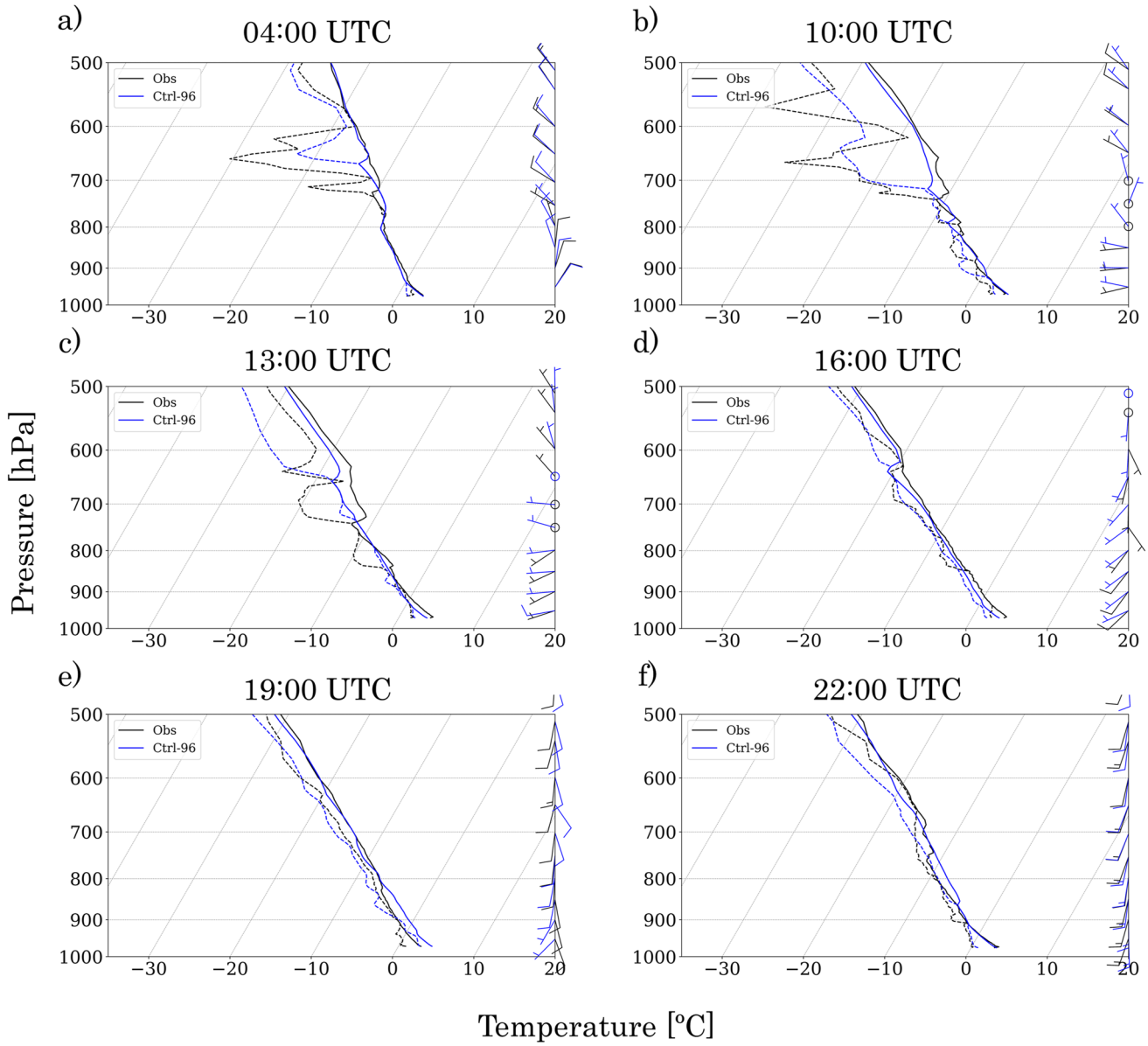

Figure 8. Mean profiles of temperature (solid line), dew point temperature (dashed line), and vector wind for shipborne observations (black) and Ctrl-96 simulations (blue), displayed as a skew T-logP diagram and wind profiles at 04 UTC (a), 10 UTC (b), 13 UTC (c), 16 UTC (d), 19 UTC (e), and 22 UTC (f), 16 Feb 2018.

motion vectors, which are then interpolated to match GPM (IMERG)'s original resolution (0.1° and 30 min) and estimate the precipitation propagation by 40 pixels (Tan et al., 2019). This morphing method has been shown to face challenges in representing short-lived or rapidly moving precipitation systems such as observed in this case study (Turk et al., 2008). Second, the PMW-only estimate is found to be less accurate over frozen surfaces and in detecting light precipitation (Naud et al., 2020; Tan et al., 2019). As 10 PWM satellites and different processing techniques (Huffman et al., 2019; Tang et al., 2020) are used for GPM (IMERG) precipitation estimates, finding the exact sources of these errors over the SO is out of the scope of our study.

While ERA5 shows some skill in identifying the peak of the precipitation during the frontal passage, it smooths it out over 10 hr instead of concentrating it in a 3-hr window, as observed by the ship. ERA5 strongly underestimates the precipitation during the cyclone period. Montoya Duque et al. (2023), constructed the Fractional Skill Score (FSS) based on the OceanPOL (e.g., C-band radar) against the ERA5 and GPM (IMERG) data and found that ERA5 has better FSS scores than IMERG at large spatial scales for precipitation thresholds between 0.07 and 0.6 mm hr^{-1}. They also noted that ERA5 commonly overestimates the frequency of precipitation and

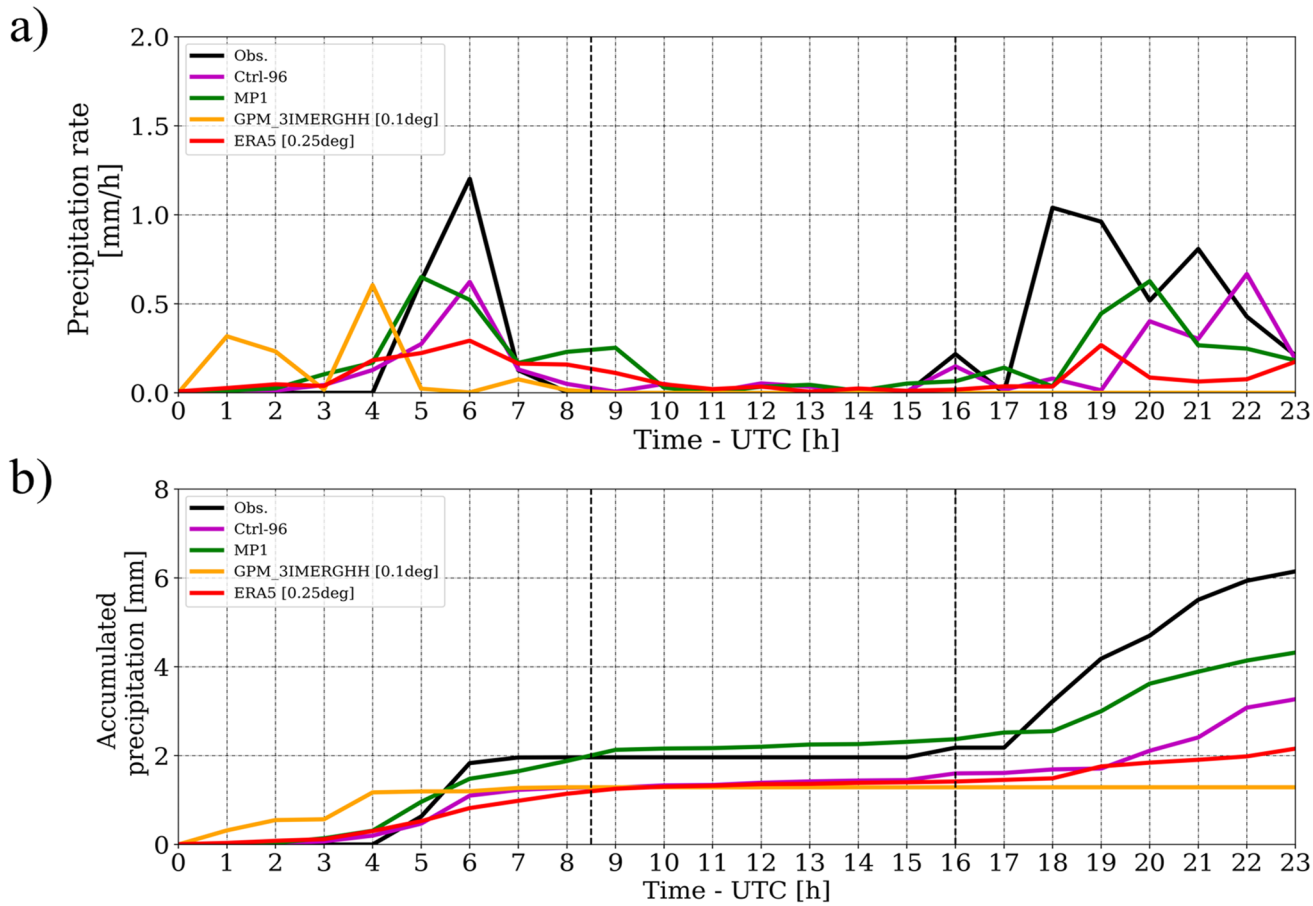

Figure 9. Time series of the observed precipitation rate and accumulated precipitation. Vertical dashed black line indicates the approximate time of the three meteorological events.

underestimates the intensity of precipitation over the SO. These high-frequency and low-intensity events are commonly referred to as the "drizzle problem", which is commonly found in Global Circulation Models and often linked to deficiencies in the parameterized convection and/or microphysics which are the two main components of precipitation estimate in the ERA5 reanalysis.

5. Numerical Simulations

High resolution WRF simulations were run with the aim of better understanding the dynamics and microphysics of this event and their interactions. For example, Section 4 suggests that ice and snow processes are likely to be important for the development of precipitation in the extra-tropical cyclone system. While a range of microphysics parameterization schemes were explored, we focus on results using the Morrison scheme (Ctrl-96) and the modified scheme following Vignon et al. (2021) (MP1).

5.1. Model Evaluation

It is worth noting again that the ERA5 reanalysis was used to provide the initial and lateral boundary conditions for all simulations. The reanalysis benefited from the CAPRICORN 2018 field campaigns because a large number of ship-based observations, such as the radiosondes uploaded to the Global Telecommunication System (GTS) of the World Weather Watch (WWW), were assimilated into it, making it available for both operational analyses and the production of the ERA5 reanalysis.

The time series of observed surface pressure, temperature, relative humidity, and winds from the ship are directly compared to the WRF simulations (Figure 10). The simulated surface pressure is well captured throughout the

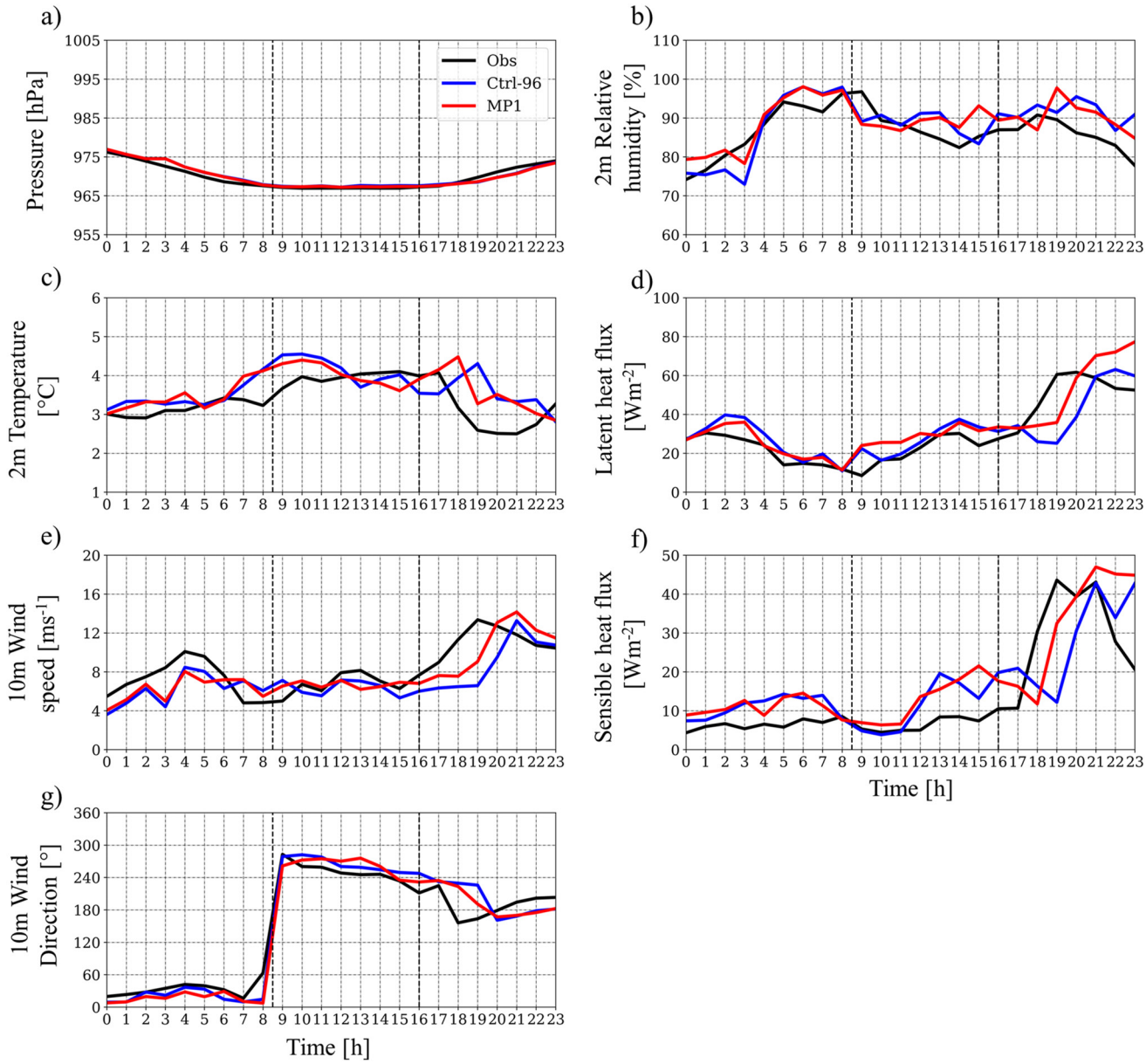

Figure 10. Time series of meteorological variables for shipborne observations, Ctrl-96 and MP1 simulations. The temporal resolution is 1 hr (a) surface pressure, (b) 2 m relative humidity, (c) 2 m air temperature (°C), (d) latent heat flux (W m^{-2}), (e) 10 m wind speed (m s^{-1}), (f) surface heat flux (W m^{-2}), (g) 10 m wind direction (°). Vertical dashed black lines indicate the approximate transition times between the three meteorological stages.

day. During the frontal and post-frontal periods, the timing of the temperature, relative humidity, and wind speed and direction is generally in good agreement with the observations. While the 10m wind speed was slightly underestimated compared to the observation, the wind speed increased from 5 to 11 m s^{-1} when the cyclone approached and remained steady around 7 m s^{-1} through the post-frontal period.

The surface wind direction jumps across the frontal boundary, from northeast to southwest, which was reproduced well by the simulations in both the timing at 08 UTC and magnitude. We found that the ERA5 wind direction changed 2 hr earlier compared to the observation and the WRF simulations (e.g., 6 UTC, Fig. S7 in Supporting Information S1). We identified two possible hypotheses to explain the better performance in WRF are (a) no nudging (e.g., spectral nudging is turned off in our simulations) and (b) the convection-permitting simulations (e.g., 1 km). First, no nudging makes WRF less reliant on large-scale meteorological fields from the ERA5 (Kanamitsu & Kanamaru, 2007). Therefore, systematic errors such as the earlier wind direction change

were not forced into the WRF simulations. Second, higher horizontal resolution allows a better representation of surface fields such as 10 m wind. The 2 m temperature and relative humidity match reasonably well (Figures 10b and 10e) through the first two stages of the event. While the simulated temperature was primarily between 3° and 4°C, it was slightly warmer (~1°C) than observed while the frontal band was passing over the ship (06–12 UTC) with a smooth transition between these two periods. The relative humidity increased gradually from ~62% to ~96% from 00 to 08 UTC. The latent heat flux was in a good agreement with observation while the sensible heat flux was slightly overestimated. During the post-frontal stage, the simulated meteorology is still found to largely agree with the observations, being largely constant throughout. We note that the 2 m relative humidity decreased slightly to below 90% during this time.

Noticeable differences are seen during the cyclone period. It appears that a ~2-hr lag has developed in the arrival of the simulated cyclone period. Also, while the observed air temperature dropped abruptly below 3°C, the simulated 2 m air temperature remained steady at around 4°C, making it 1–2°C warmer than observed. While this difference may be relatively small, it can have a significant impact on the sensible and latent heat fluxes. The models underestimate both sensible and latent heat fluxes during this period (Figures 10d and 10f) suggesting that the simulated convection is weaker than observed (e.g., shallower cloud top heights). The simulated relative humidity is also higher than observed by 10%, lowering the latent heat flux compared with observations. Toward the end of the simulation, after the arrival of the cyclone period, the simulated and observed winds are seen to largely return to reasonable agreement. Overall, the frontal passage and post-frontal stages are well captured by the simulations, whereas a timing/location lag is found toward the end of the simulation with the arrival of the cyclone period (Figure 10). We found that longer spin-up time results in larger biases in the simulated near-surface thermodynamic variables suggesting that the WRF's performance depends more on the initial condition and has less constraint on the boundary conditions. The sensitivity of spin-up time had also been discussed in Atlas et al. (2020), where they highlighted that 12–14 hr were long enough to retain realistic turbulence and boundary layer height in simulating the low-level cloud over the SO in summertime.

Next the simulated sounding profiles are compared with upper-air soundings (Figure 8). As the radiosonde launched during the CAPRICORN 2018 were assimilated into the ERA5 reanalysis, a high degree of skill is expected in the simulated soundings at the start of the simulations, particularly through the lower troposphere (Figure 8a). Looking a little later near the frontal passage (10 UTC), the CTRL simulation still shows considerable skill (Figure 8b).

For the post-frontal period (Figures 8c and 8d), the simulations start to drift away from the observations, potentially introducing errors in the timing and location of various features. The simulations suggest a deep moist layer from the surface to 650 hPa, rather than three distinct saturation layers observed at 900, 850, and 750 hPa. The dewpoint temperature and temperature are ~2°C lower than the observed (Figure 8c) from the surface up to 850 hPa (Figure 8d). The simulated wind profiles started deviating from the observations, shearing from the southwest at the surface to the northwest above 700 hPa. The simulations tend to vertically smooth the fields during this period.

Turning to the cyclone period (Figures 8e and 8f), the simulated temperature is ~2°C warmer than the observed up to 700 hPa (Figure 8e). Moreover, the simulation fails to develop the observed wind shear. While the observed wind direction changed from southeast to southwest from surface to 500 hPa, it changed from southwest to southeast in the model simulation (Figure 8e). This suggests that the location of the cyclone (relative to the ship) is different between the simulation and the observation (e.g., the timing/spatial offset of the cyclone period, Figure 10h).

Figure 9 shows the observed and modeled precipitation rate and accumulated precipitation. Ctrl-96 reproduced the timing of the peak near 06 UTC but underestimated the magnitude of the precipitation during the frontal passage. While virtually no precipitation was observed during the post-frontal period (10–16 UTC), the simulation reproduced this precipitation-free slot right after the front. Notable differences are seen in accumulated precipitation between the simulation (~1.5 mm) and observation (~4 mm) during the cyclone period with the onset of the precipitation lagged by an hour in the simulation.

Figure 11 shows the vertical profiles of mixing ratios of different hydrometeor species taken from the Ctrl-96, MP1 simulations, and ERA5 reanalysis. These cannot be compared directly against the cloud phase product (Figure 4c), but ideally would have similar macrophysics. The temporal resolution is 1 hr and the nearest grid

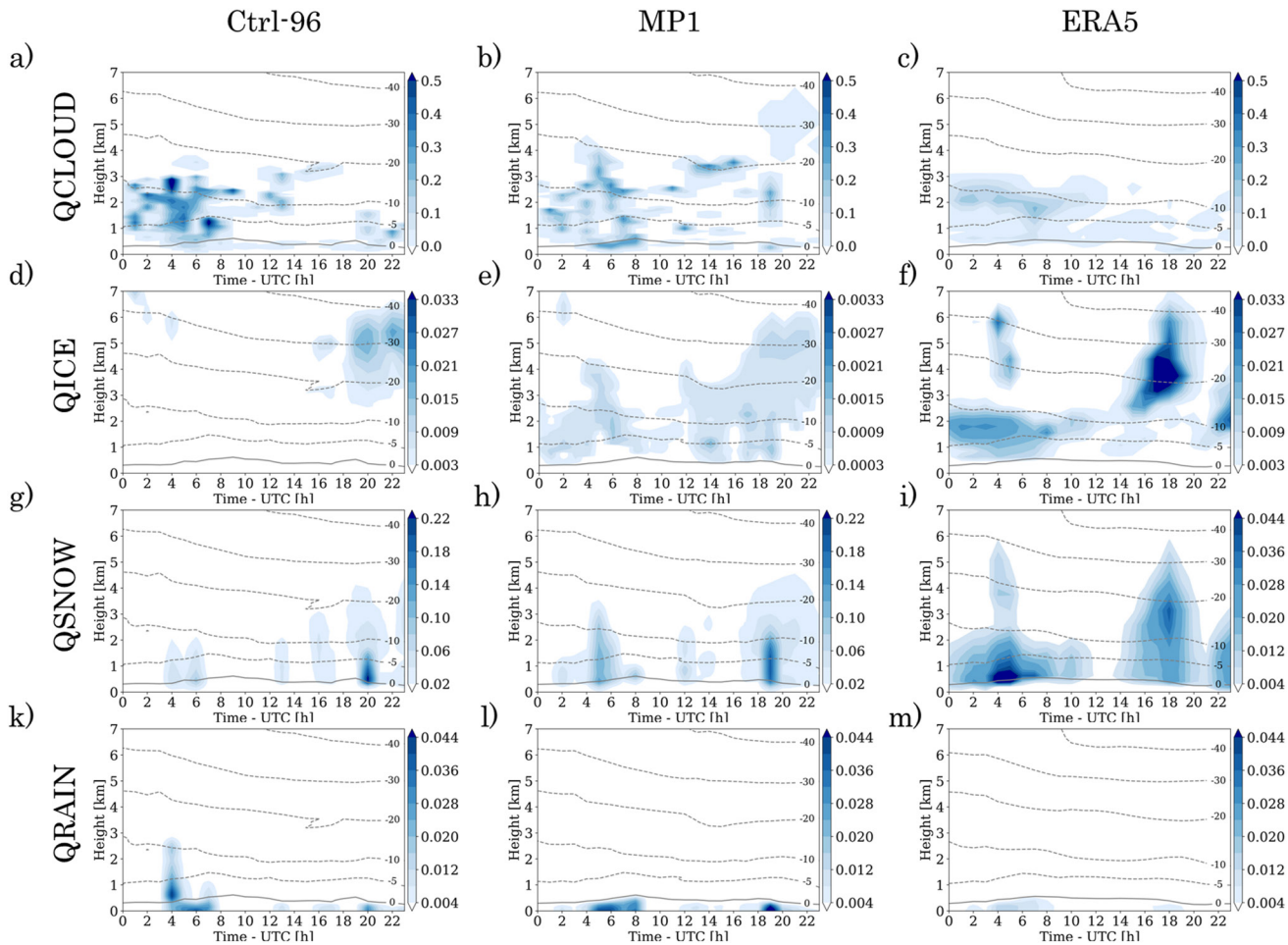

Figure 11. Vertical profiles of the mixing ratios (g kg^{-1}) of (a) liquid cloud (b) ice (c) snow, and (d) rain for Ctrl-96 (leftmost), MP1 (middle) and ERA5 (rightmost). The temporal resolution is 1 hr. A different color bar is used in panels (b) and (c) Vertical dashed black line indicates the approximate time of the three meteorological events.

point to the ship location is used for all panels. We include ERA5 in this comparison as a simple means to comment on the sensitivity of cloud amount to the vertical resolution. Since ice and snow are defined differently in WRF and ERA5, a direct quantitative comparison between the two is inappropriate. Rather we consider the differences in the boundaries.

During the frontal passage, Ctrl-96 produced a cloud top height at ~3 km, much lower than that observed by the BASTA and OceanPOL radar. While Ctrl-96 produced a large amount of cloud water and snow, it also indicates that no cloud ice is present during this period, which suggests that auto-conversion from ice to snow and/or accretion of ice to form snow above the freezing level are enhanced in Ctrl-96, leading to a higher depletion of cloud ice during the frontal passage (Figure 11d). There is freezing rain at 04 UTC (Figure 11k) in Ctrl-96, which could be due to the auto-conversion of cloud water to raindrops.

During the postfrontal period, Ctrl-96 struggled to reproduce the multi-layer cloud structure, particularly the topmost SLW cloud layer at 2.3 km. While the observations suggest it was an extended SLW cloud layer, Ctrl-96 produced a sporadic cloud water pattern whose CTHs could reach approximately 4 km ASL. The surface cloud layer (up to ~500 m) was reasonably well produced by Ctrl-96. Through this period, the poor representation of cloud structure is evident in the ERA5 cloud product.

The height of cloud ice during the cyclone period in Ctrl-96 (Figure 11d) was approximately 6.5 km ASL at 18 UTC, which again suggests a 2-hr delay of the cyclone in the simulation (Figure 4). During the cyclone period, Ctrl-96 suggests there is little liquid cloud present in the upper troposphere while a significant amount of cloud

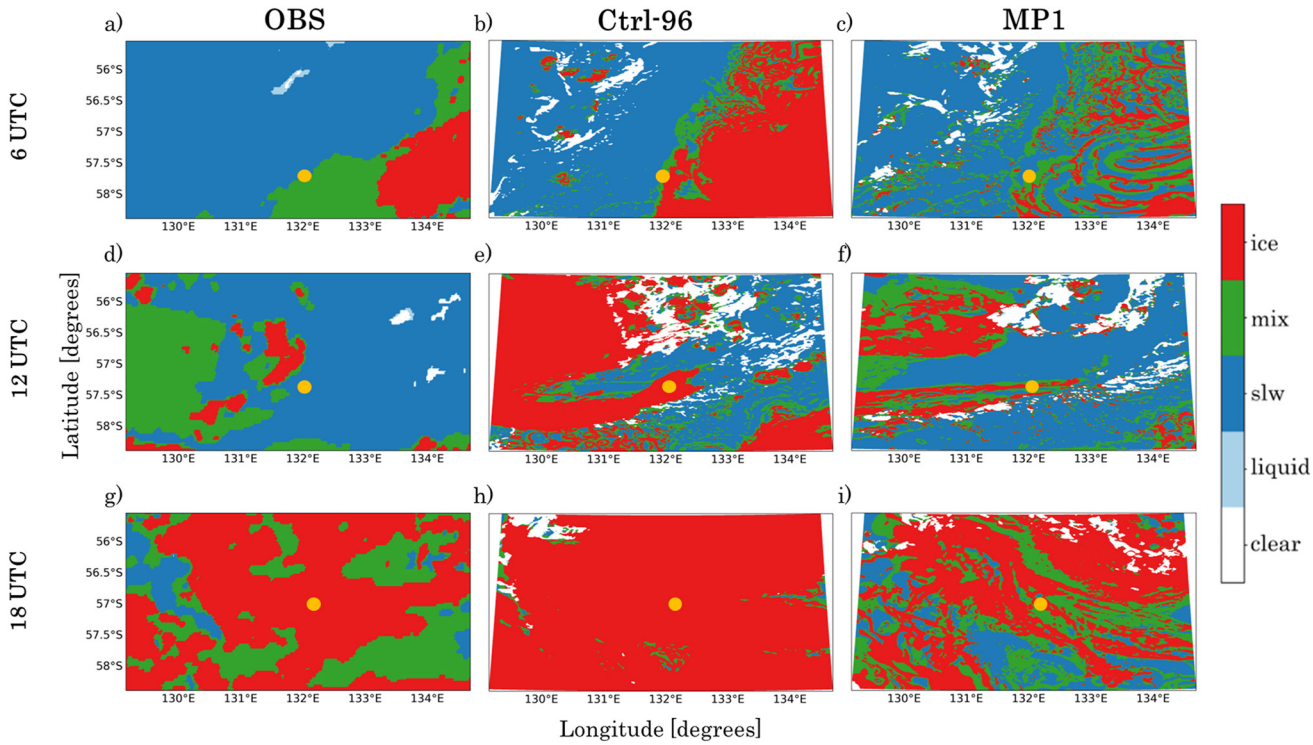

Figure 12. Himawari-8 observed (left), the WRF (1 km resolution simulations) Ctrl (middle), and MP1 (right) simulated CTTs.

ice formed after 18 UTC. Finally, the CFAD diagram constructed by Ctrl-96 indicates that the simulation failed to produce convection above 3 km in both frontal and cyclone periods (Figures 7b and 7e)—well below the observed cloud depth. We found the height of the convection as seen in Figure 7e remains unchanged when plotting the CFAD diagram at 20 UTC. As such, this bias of convection height could be linked to other dynamic factors such as winds (Figure 8e).

Figure 12 shows the simulated CTPs from the Ctrl-96 at 06, 12, and 18 UTC on 16 Feb 2018. Simulated CTPs are defined by Huang et al. (2014) diagnostic method, which is based on the relative fraction of liquid water to total water at 0.01 optical depth from the cloud top. For the frontal passage (Figures 12a–12c), the observed CTPs were largely dominated by the SLW with mixed phase and ice cloud located east and southeast of the ship. Ctrl-96 reproduced the SLW well but overestimated the amount of ice cloud. In the post-frontal period, a large amount of SLW was again observed, with little evidence of glaciation. A mixed-phased cloud was observed toward the west. In contrast, Ctrl-96 produced excessive amount of ice. Turning to the cyclone period (Figures 12g–12i), Ctrl-96 simulated cloud tops are entirely glaciated, whereas there is a mixture of ice and mixed phased clouds observed.

The Himawari-8 CTP at 06, 12, and 18 UTC (Figures 12a, 12d, & 12g) largely agrees with the merged radar and lidar CTP (Figure 3c), particularly when SLW was recorded during the post-frontal period near 12 UTC. The Ctrl-96 simulated CTPs was largely ice rather than SLW or mixed phase was produced by Ctrl-96, which suggests the enhancement of ice production at the expense of SLW cloud.

5.2. Model Sensitivity

The time series of simulated surface pressure, temperature, relative humidity and winds from Ctrl-96 are comparable to MP1. The accumulated precipitation is better captured by MP1 than Ctrl-96 (Figure 9). During the frontal passage, MP1 reproduced a larger cloud amount with the CTHs is roughly 4 km. Ice cloud formed in the upper levels is conversed/accreted to snow in the lower layer. This process could be a signature of the seeder-feeder process where upper-level precipitating ice cloud seeds the lower water cloud (Alexander et al., 2021). We noted that Ctrl-96 simulates freezing drizzle/rain from 0°C to −10°C isotherm, while MP1 produced a higher snow mass concentration in this layer compared to Ctrl-96 (Figures 11h and 11k). As a result, MP1 produced a higher amount of rain at the surface from snowmelt compared to Ctrl-96 (Figures 9a and 9b, Figures 11k–11l).

Moving on to the cyclone period, marked differences are seen in the simulated precipitation, particularly the simulated precipitation rates. While the ODM suggests there are precipitation peaks at 18 and 21 UTC, neither of the simulations can reproduce reasonable timing and comparable amount. MP1 produced a deeper layer of snow with mass concentrations exceeding 0.15 g kg^{-1} (up to 2 km) compared to Ctrl-96 (up to 1.5 km). Analogous to the frontal passage, higher amount of rain due to snow melting is seen in MP1 (Figures 9a and 9b, Figure 11d). In contrast to Ctrl-96, the cloud top phase in MP1 is more realistic when compared to the Himawari-8 (Figure 12i). This suggests that lowering INPs concentration in the model could be important in simulating clouds and consequently precipitation during the cyclone period. Moving to the upper-troposphere where the temperature is colder than −15°C, MP1 shows significantly smaller ice number concentration compared to Ctrl-96 during the post-frontal and cyclone periods (Fig. S8 in Supporting Information S1). The higher ice number concentration in Ctrl-96 was previously reported in Vignon et al. (2021) (their Fig. S2 and S9) where the immersion freezing nucleation was found to be a dominant ice production mode in the control simulation, notably at temperatures below 15°C. This further highlights the importance of low INP concentrations in governing the ice formation processes at the cloud top.

In summary, we found that MP1 reproduced a larger amount of snow and ice between −3 and −10°C temperature range compared to Ctrl-96 during both frontal and cyclone periods. The higher amount of snow suggests that accretion of cloud droplets onto snow due to a larger availability of SLW in a lower INPs atmosphere is enhanced in MP1. On the other hand, the higher amount of ice is more likely associated with the rime-splintering process (Hallett Mossop), which is the only parameterization of secondary ice production in the Morrison microphysics scheme (Morrison et al., 2005). In Morrison et al. (2005), new ice particles (e.g., secondary ice particles) can splinter from rimed particles at temperatures between −3 and −8°C when either the cloud water mixing ratio is larger than 0.5 g kg^{-1}or rain water mixing ratio is larger than 0.1 g kg^{-1}. Rime splintering can occur on snow and/or graupel (negligible amount in our case study) if their mixing ratio is larger than 0.1 g kg^{-1}. We noted that the splintering from droplets accreted onto snow is a function of rimed particles (e.g., accretion of cloud droplets onto snow) and temperature (e.g., different rates from −8° to −5° and −5° to −3°C). Therefore, we speculate that the enhancement of the accretion of cloud droplets onto snow in MP1 enhanced the secondary ice process (Hallett Mossop). The higher ice number concentrations (QNICE) simulated by MP1 and Ctrl-96 (Fig. S7 in Supporting Information S1) further support our speculation. MP1 simulates higher ice number concentrations between the −3 and −10°C temperature ranges. Therefore, the ice crystals produced by rime splintering in MP1 further grow into snow and graupel through riming, aggregation, and deposition. Subsequently, the higher ice water content in MP1 compared to Ctrl-96 produced stronger rain rates at the surface due to melting. The higher rain rates simulated by MP1 were closer to the observations.

Overall, the results suggest the synoptic scale cloud was relatively well simulated, but the cloud top phase is highly sensitive to the microphysics package. Finally, we further examined the diagnosed reflectivity from CR-SIM and found that snow was largely present at both above and below freezing level during both the frontal passage and cyclone period (negligibly small amount of diagnosed reflectivity due to ice and graupel).

6. Discussion and Conclusions

In this study, we used the shipborne measurements from the CAPRICORN 2018 field campaign, which includes C-band radar observations, to investigate the characteristics and variability of precipitation across different sectors of an extra-tropical cyclone over the high latitudes of the Southern Ocean (SO). This event was noteworthy as being the second heaviest rainfall "day" encountered during the campaign with a variety of precipitation mechanisms present. We separated this day into three different periods: the prefrontal and frontal passage (00–09 UTC), post-frontal period (09–16 UTC) and high-latitude cyclone (15–24 UTC). Precipitation was observed during both the frontal passage and the cyclone period, but not the post-frontal period.

During the frontal stage, the ODM detected precipitation from 05 to 07 UTC, with a peak rate of 3.0 mm hr^{-1} and a total accumulation of 1.9 mm. The BASTA radar suggests the freezing level was shallow at around 500 m, where a sharp transition in the Doppler vertical velocity is evident. Our results show that snow was largely presents above the freezing level whereas 96% of precipitation below the freezing level is recorded as rain as by the ODM. The highest observed CTHs as observed by the C-band radar were approximately 6.5 km. The ship technically encountered a warm front rather than a cold front, as the pre-frontal air mass was the remnants of a

cold air outbreak event. The sensible and latent heat fluxes were weak (<50 W m^{-2} combined), dropping to near zero over the actual frontal passage.

The post-frontal period was defined by a non-precipitating multi-layer cloud structure. A geometrically thin (~200 m) uniform layer of SLW cloud overlayed shallow boundary layer convection. The net surface heat flux increased during this period but remained relatively weak (under 50 W m^{-2}). A statically unstable environment and warmer SST supported these shallow low-level convective clouds (<1 km). Horizontal shear/warm air advection produced the upper cloud layer at 2.3 km. Such thin SLW cloud layers have previously been reported over the Southern Ocean (Chubb et al., 2013).

Finally, the high-latitude cyclone core was encountered during which the heaviest precipitation (~4 mm accumulation) was recorded. The precipitation phase varied with snow (10%) and mixed phase (40%) recorded. On average the clouds were shallower in this period than during the frontal period, although deeper cloud depths of ~6 km were sporadically recorded (Figures 5 and 6). The surface latent heat flux more than doubled to about 60 Wm^{-2} and the sensible heat flux increased from 10 to 40 Wm^{-2}. The increased surface fluxes and the southerly wind direction suggest that the precipitation in the cyclone was being driven by cold air advection, presumably from Antarctica, rather than warm air advection from lower latitudes.

We presented the ERA5 and GPM (IMERG) precipitation given the uniqueness of the observations and meteorology. While both products roughly captured the precipitation during the frontal passage, both strongly underestimated the precipitation rate during the cyclone. A detailed investigation of the potential causes of these biases is beyond the scope of this paper, although we note the error of GPM (IMERG) in our case study could be due to either the poor performance of passive microwave estimations (Tan et al., 2017) or the classification of rain and snow, which was simply based on the wet-bulb temperature with a constant temperature threshold across the globe (Tang et al., 2020).

The ship-borne observations were used to evaluate high-resolution WRF simulations, specifically a control simulation (Ctrl-96) using the Morrison microphysics scheme and a variant (MP1) of this scheme (Vignon et al., 2021) that adapted a new ice nucleation parameterization where concentration of INPs is less than other current heterogeneous nucleation parameterizations operated in WRF (e.g., Bigg, 1953; Cooper, 1986; Meyers et al., 1992). We did a number of other sensitivity studies including Thompson microphysics scheme (e.g., only default microphysical setting run), Mellor-Yamada-Nakanishi-Niino planetary boundary layer scheme (e.g., using local closure scheme), but they did not substantially improve the precipitation simulation and particularly the depth of the convection in our case study.

Although both simulations are relatively skillful in representing surface meteorology, particularly during the frontal and post-frontal periods, the simulations showed less skill during the cyclone period. While the Himawari-8 satellite product suggests an extensive field of frontal clouds, which largely consisted of SLW, the Ctrl-96 simulation struggled to reproduce the cloud morphology, cloud depth and microphysical characteristics with an excessive amount of ice cloud. A timing/spatial offset of 1–2 hr is evident in the WRF simulations at the onset of the cyclone period.

In general, the simulated CBH agrees with the observations, whereas the simulated CTHs were too shallow (50%). The simulations largely failed to reproduce the multi-layer cloud structure during the post-frontal period, especially the topmost layer at 2.3 km. The Ctrl-96 is found to produce excessive amount of ice cloud at the cloud top, while larger quantities of SLW clouds are seen in MP1. Still, both Ctrl-96 and MP1 produced less precipitation in comparison to observations during the cyclone period. This last period, when the strongest precipitation occurred, was predominantly driven by strong surface fluxes. We noted that both simulations also failed to produce convection above 3 km in both frontal and cyclone periods (Figures 6b and 6e).

Although we demonstrated that better representation of INPs in MP1 produced more skilled simulations of CTPs and the near-surface thermodynamic variables, more work still needs to be done to improve the cloud and their microphysical phases over the Southern Ocean. In fact, lower INPs parameterization largely reflects immersion freezing, which commonly happens at temperatures lower than −15°C. Hence, low INPs cannot fully explain the glaciation of low-level clouds (McCluskey et al., 2018), where multiplication of frozen hydrometeors can take place through different secondary ice processes (SIP). Järvinen et al. (2022) reported that observed ice crystal concentrations were one to two orders of magnitude higher than simultaneously measured INP concentrations below 10°C and up to five orders of magnitude higher than estimated INP concentrations above 10°C. They also

noted that the rate of ice production is faster than what was measured from the Hallett and Mossop (1974) study, which meant that there are other SIP mechanisms beyond the Hallett-Mossop active at lower temperatures. As such, further research is necessary to learn more about SIP, potentially ice-ice collisions (Georgakaki et al., 2022; Sotiropoulou et al., 2020), and droplet fragmentation (Korolev et al., 2020) during freezing (Fig., 13, in Järvinen et al., 2022). This will not only improve the mixed-phase cloud simulation but also precipitation forecasts as well as the phases of precipitation, for example, freezing drizzle/rain versus snow and graupel.

Despite being a single case study, this represents a unique set of observations to study the characteristics and variability of precipitation across different sectors of an extra-tropical cyclone over the high-latitudes of the SO. Our analysis emphasizes the role of ice processes at sub-freezing temperatures in the development of precipitation in these clouds and the complex thermodynamics and the potential role of horizontal advection and vertical wind shear in forming the multi-layer cloud structure after the frontal passage. As shown by the model simulations, the frontal precipitation intensity is fairly reproduced while it is underestimated during the cyclone period. This high-latitude cyclone was able to produce significant precipitation and deep clouds from relatively strong surface fluxes. This bias may contribute to the precipitation uncertainty at the high latitude of the SO (Behrangi & Song, 2020; Manton et al., 2020).

Data Availability Statement

The CAPRICORN II data used in this case study including the merged cloud radar-lidar product, OceanRain (ODM), BASTA cloud radar, surface meteorological observations [Protat, Alain; CSIRO; Marine National Facility (2020); UCAR/NCAR EOL (2018)]. The OceanPOL V2020 weather radar is available on the National Computing Infrastructure (NCI) (Louf and Protat (2020)). The ERA5 hourly data on single levels from 1940 to present can be downloaded from (Hersbach et al., 2023). The GPM (IMERG) Precipitation can be downloaded from (Huffman et al., 2019). The ERA5 and GPM (IMERG) are findable and accessible through user registration. The WRF model source code is available at (https://www2.mmm.ucar.edu/wrf/users/download/get_source.html). The WRF model namelist can be downloaded at (Truong (2023)). The post-processing software "Cloud Resolving Model Radar Simulator" is available at (https://www.bnl.gov/cmas/cr-sim.php). The HYSPLIT, online internet-based interface, can be accessed at (https://www.ready.noaa.gov/HYSPLIT.php). All references of the datasets are listed in the in-text data citation references.

Acknowledgments
This work is supported by an Australian Research Council discovery grant DP190101362. The authors deeply thank the entire CAPRICORN, MARCUS, MICRE, and SOCRATES teams for their tremendous efforts and dedication in collecting the data sets. We acknowledge the use of the CSIRO Marine National Facility (https://ror.org/01mae9353) and grant of sea time on RV Investigator in undertaking this research. We greatly appreciate Emeritus Prof. Michael Manton and Prof. Michael Reeder from Monash University for insightful comments on the work. We acknowledge Alain Protat and Valentine Louf for their work in preparing the OceanPOL data. We thank Estefania Montoya Duque for valuable discussion on the GPM (IMERG) and ERA5 precipitation dataset. Lastly, we thank the three reviewers' thoughtful suggestions, which helped us improve our paper.

References

Ahn, E., Huang, Y., Chubb, T. H., Baumgardner, D., Isaac, P., De Hoog, M., et al. (2017). In situ observations of wintertime low-altitude clouds over the Southern Ocean. *Quarterly Journal of the Royal Meteorological Society*, *143*(704), 1381–1394. https://doi.org/10.1002/qj.3011

Alexander, S., McFarquhar, G., Marchand, R., Protat, A., Vignon, É., Mace, G., & Klekociuk, A. (2021). Mixed-phase clouds and precipitation in Southern Ocean cyclones and cloud systems observed poleward of 64°S by ship-based cloud radar and lidar. *Journal of Geophysical Research: Atmospheres*, *126*(8), e2020JD033626. https://doi.org/10.1029/2020jd033626

Atlas, R., Bretherton, C. S., Blossey, P. N., Gettelman, A., Bardeen, C., Lin, P., & Ming, Y. (2020). How well do large-eddy simulations and global climate models represent observed boundary layer structures and low clouds over the summertime Southern Ocean? *Journal of Advances in Modeling Earth Systems*, *12*(11), e2020MS002205. https://doi.org/10.1029/2020ms002205

Atlas, R. L., Bretherton, C. S., Blossey, P. N., Gettelman, A., Bardeen, C., Lin, P., & Ming, Y. (2020). How well do large-eddy simulations and global climate models represent observed boundary layer structures and low clouds over the summertime Southern Ocean? *Journal of Advances in Modeling Earth Systems*, *12*(11), e2020MS00220. https://doi.org/10.1029/2020MS002205

Behrangi, A., Christensen, M., Richardson, M., Lebsock, M., Stephens, G., Huffman, G. J., et al. (2016). Status of high-latitude precipitation estimates from observation and reanalyses. *Journal of Geophysical Research: Atmospheres*, *121*(9), 4468–4486. https://doi.org/10.1002/2015JD024546

Behrangi, A., & Song, Y. (2020). A new estimate for oceanic precipitation amount and distribution using complementary precipitation observations from space and comparison with GPCP. *Environmental Research Letters*, *15*(12), 124042. https://doi.org/10.1088/1748-9326/abc6d1

Bigg, E. K. (1953). The supercooling of water. *Proceedings of the Physical Society Section B*, *66*(8), 688–694. https://doi.org/10.1088/0370-1301/66/8/309

Boisvert, L. N., Webster, M. A., Petty, A. A., Markus, T., Cullather, R. I., & Bromwich, D. H. (2020). Intercomparison of precipitation estimates over the Southern Ocean from atmospheric reanalyses. *Journal of Climate*, *33*(24), 10627–10651. https://doi.org/10.1175/jcli-d-20-0044.1

Chubb, T. H., Jensen, J. B., Siems, S. T., & Manton, M. J. (2013). In situ observations of supercooled liquid clouds over the Southern Ocean during the HIAPER pole-to-pole observation campaigns. *Geophysical Research Letters*, *40*(19), 5280–5285. https://doi.org/10.1002/grl.50986

Cooper, W. A. (1986). Ice initiation in natural clouds. *Meteorological Monographs*, *21*(43), 29–32. https://doi.org/10.1175/0065-9401-21.43.29

Dong, S., Sprintall, J., & Gille, S. T. (2006). Location of the Antarctic polar front from AMSR-E satellite sea surface temperature measurements. *Journal of Physical Oceanography*, *36*(11), 2075–2089. https://doi.org/10.1175/JPO2973.1

Fletcher, J. K., Mason, S., & Jakob, C. (2016a). The climatology, meteorology, and boundary layer structure of marine cold air outbreaks in both hemispheres. *Journal of Climate*, *29*(6), 1999–2014. https://doi.org/10.1175/JCLI-D-15-0268.1

Fletcher, J. K., Mason, S., & Jakob, C. (2016b). A climatology of clouds in marine cold air outbreaks in both hemispheres. *Journal of Climate*, *29*(18), 6677–6692. https://doi.org/10.1175/JCLI-D-15-0783.1

Georgakaki, P., Sotiropoulou, G., Vignon, É., Billault-Roux, A.-C., Berne, A., & Nenes, A. (2022). Secondary ice production processes in wintertime alpine mixed-phase clouds. *Atmospheric Chemistry and Physics*, *22*(3), 1965–1988. https://doi.org/10.5194/acp-22-1965-2022

Gordon, A. E., Cavallo, S. M., & Novak, A. K. (2023). Evaluating common characteristics of Antarctic tropopause polar vortices. *Journal of the Atmospheric Sciences*, *80*(1), 337–352. https://doi.org/10.1175/JAS-D-22-0091.1

Hallett, J., & Mossop, S. (1974). Production of secondary ice particles during the riming process. *Nature*, *249*(5452), 26–28. https://doi.org/10.1038/249026a0

Heidinger, A. K. (2011). *ABI cloud height algorithm (ACHA) algorithm theoretical basis document (ATBD)*. GOES-R Program Office.

Hersbach, H., Bell, B., Berrisford, P., Biavati, G., Horányi, A., Muñoz Sabater, J., et al. (2023). ERA5 hourly data on single levels from 1940 to present. [Dataset]. Copernicus Climate Change Service (C3S) Climate Data Store (CDS). https://doi.org/10.24381/cds.adbb2d47

Hersbach, H., Bell, B., Berrisford, P., Hirahara, S., Horányi, A., Muñoz-Sabater, J., et al. (2020). The ERA5 global reanalysis. *Quarterly Journal of the Royal Meteorological Society*, *146*(730), 1999–2049. https://doi.org/10.1002/qj.3803

Hong, S.-Y., Noh, Y., & Dudhia, J. (2006). A new vertical diffusion package with an explicit treatment of entrainment processes. *Monthly Weather Review*, *134*(9), 2318–2341. https://doi.org/10.1175/mwr3199.1

Hu, Y., Rodier, S., Xu, K. m., Sun, W., Huang, J., Lin, B., et al. (2010). Occurrence, liquid water content, and fraction of supercooled water clouds from combined CALIOP/IIR/MODIS measurements. *Journal of Geophysical Research*, *115*(D4). https://doi.org/10.1029/2009jd012384

Huang, Y., Siems, S. T., & Manton, M. J. (2021). Wintertime in situ cloud microphysical properties of mixed-phase clouds over the Southern Ocean. *Journal of Geophysical Research: Atmospheres*, *126*(11), e2021JD034832. https://doi.org/10.1029/2021jd034832

Huang, Y., Siems, S. T., Manton, M. J., Protat, A., & Delanoë, J. (2012). A study on the low-altitude clouds over the Southern Ocean using the DARDAR-MASK. *Journal of Geophysical Research*, *117*(D18). https://doi.org/10.1029/2012jd017800

Huang, Y., Siems, S. T., Manton, M. J., & Thompson, G. (2014). An evaluation of WRF simulations of clouds over the Southern Ocean with a-train observations. *Monthly Weather Review*, *142*(2), 647–667. https://doi.org/10.1175/mwr-d-13-00128.1

Huffman, G. J., Stocker, E. F., Bolvin, D. T., Nelkin, E. J., & Tan, J. (2019). GPM IMERG final precipitation L3 1 day 0.1 degree x 0.1 degree V06. In A. Savtchenko & M. D. Greenbelt (Eds.), *Goddard earth sciences data and information services center (GES DISC)*. https://doi.org/10.5067/GPM/IMERGDF/DAY/06

Iacono, M. J., Delamere, J. S., Mlawer, E. J., Shephard, M. W., Clough, S. A., & Collins, W. D. (2008). Radiative forcing by long-lived greenhouse gases: Calculations with the AER radiative transfer models. *Journal of Geophysical Research*, *113*(D13). https://doi.org/10.1029/2008jd009944

Järvinen, E., McCluskey, C. S., Waitz, F., Schnaiter, M., Bansemer, A., Bardeen, C. G., et al. (2022). Evidence for secondary ice production in southern ocean maritime boundary layer clouds. *Journal of Geophysical Research: Atmospheres*, *127*(16), e2021JD036411. https://doi.org/10.1029/2021JD036411

Kanamitsu, M., & Kanamaru, H. (2007). Fifty-seven-Year California reanalysis downscaling at 10 km (CaRD10). Part I: System detail and validation with observations. *Journal of Climate*, *20*(22), 5553–5571. https://doi.org/10.1175/2007JCLI1482.1

Klepp, C., Michel, S., Protat, A., Burdanowitz, J., Albern, N., Kähnert, M., et al. (2018). OceanRAIN, a new in-situ shipboard global ocean surface-reference dataset of all water cycle components. *Scientific Data*, *5*(1), 1–22. https://doi.org/10.1038/sdata.2018.122

Korolev, A., Heckman, I., Wolde, M., Ackerman, A. S., Fridlind, A. M., Ladino, L. A., et al. (2020). A new look at the environmental conditions favorable to secondary ice production. *Atmospheric Chemistry and Physics*, *20*(3), 1391–1429. https://doi.org/10.5194/acp-20-1391-2020

Korolev, A., & Leisner, T. (2020). Review of experimental studies of secondary ice production. *Atmospheric Chemistry and Physics*, *20*(20), 11767–11797. https://doi.org/10.5194/acp-20-11767-2020

Lang, F., Ackermann, L., Huang, Y., Truong, S. C., Siems, S. T., & Manton, M. J. (2022). A climatology of open and closed mesoscale cellular convection over the Southern Ocean derived from Himawari-8 observations. *Atmospheric Chemistry and Physics*, *22*(3), 2135–2152. https://doi.org/10.5194/acp-22-2135-2022

Lang, F., Huang, Y., Protat, A., Truong, S., Siems, S., & Manton, M. (2021). Shallow convection and precipitation over the Southern Ocean: A case study during the CAPRICORN 2016 field campaign. *Journal of Geophysical Research: Atmospheres*, *126*(9), e2020JD034088. https://doi.org/10.1029/2020jd034088

Lang, F., Huang, Y., Siems, S. T., & Manton, M. J. (2020). Evidence of a diurnal cycle in precipitation over the Southern Ocean as observed at Macquarie island. *Atmosphere*, *11*(2), 181. https://doi.org/10.3390/atmos11020181

Lasher-Trapp, S., Scott, E. L., Järvinen, E., Schnaiter, M., Waitz, F., DeMott, P. J., et al. (2021). Observations and modeling of rime splintering in Southern Ocean cumuli. *Journal of Geophysical Research: Atmospheres*, *126*(23), e2021JD035479. https://doi.org/10.1029/2021JD035479

Louf, V., & Protat, A. (2020). OceanPOL weather radar dataset. [Dataset]. National Computing Infrastructure. https://doi.org/10.25914/5fc4975c7dda8

Mace, G. G., Protat, A., Humphries, R. S., Alexander, S. P., McRobert, I. M., Ward, J., et al. (2021). Southern Ocean cloud properties derived from CAPRICORN and MARCUS data. *Journal of Geophysical Research: Atmospheres*, *126*(4), e2020JD033368. https://doi.org/10.1029/2020jd033368

Mace, G. G., Zhang, Q., Vaughan, M., Marchand, R., Stephens, G., Trepte, C., & Winker, D. (2009). A description of hydrometeor layer occurrence statistics derived from the first year of merged Cloudsat and CALIPSO data. *Journal of Geophysical Research*, *114*(D8). https://doi.org/10.1029/2007jd009755

Manton, M., Huang, Y., & Siems, S. (2020). Variations in precipitation across the Southern Ocean. *Journal of Climate*, *33*(24), 10653–10670. https://doi.org/10.1175/jcli-d-20-0120.1

McCluskey, C. S., Hill, T. C. J., Humphries, R. S., Rauker, A. M., Moreau, S., Strutton, P. G., et al. (2018). Observations of ice nucleating particles over Southern Ocean waters. *Geophysical Research Letters*, *45*(21), 11989–11997. https://doi.org/10.1029/2018GL079981

McCoy, I. L., Bretherton, C. S., Wood, R., Twohy, C. H., Gettelman, A., Bardeen, C. G., & Toohey, D. W. (2021). Influences of recent particle formation on Southern Ocean aerosol variability and low cloud properties. *Journal of Geophysical Research: Atmospheres*, *126*(8), e2020JD033529. https://doi.org/10.1029/2020JD033529

McFarquhar, G. M., Bretherton, C. S., Marchand, R., Protat, A., DeMott, P. J., Alexander, S. P., et al. (2021). Observations of clouds, aerosols, precipitation, and surface radiation over the Southern Ocean: An Overview of CAPRICORN, MARCUS, MICRE, and SOCRATES. *Bulletin of the American Meteorological Society*, *102*(4), E894–E928. https://doi.org/10.1175/bams-d-20-0132.1

Messmer, M., & Simmonds, I. (2021). Global analysis of cyclone-induced compound precipitation and wind extreme events. *Weather and Climate Extremes*, *32*(100324), 2021. ISSN 2212-0947. https://doi.org/10.1016/j.wace.2021.100324

Meyers, M. P., DeMott, P. J., & Cotton, W. R. (1992). New primary ice-nucleation parameterizations in an explicit cloud model. *Journal of Applied Meteorology and Climatology*, *31*(7), 708–721. https://doi.org/10.1175/1520-0450(1992)031<0708:npinpi>2.0.co;2;2

Mishchenko, M. I., & Travis, L. D. (1998). Capabilities and limitations of a current FORTRAN implementation of the T-matrix method for randomly oriented, rotationally symmetric scatterers. *Journal of Quantitative Spectroscopy and Radiative Transfer*, *60*(3), 309–324. https://doi.org/10.1016/S0022-4073(98)00008-9

Mlawer, E. J., Taubman, S. J., Brown, P. D., Iacono, M. J., & Clough, S. A. (1997). Radiative transfer for inhomogeneous atmospheres: RRTM, a validated correlated-k model for the longwave. *Journal of Geophysical Research*, *102*(D14), 16663–16682. https://doi.org/10.1029/97jd00237

Montoya Duque, E., Huang, Y., May, P. T., & Siems, S. (2023). An evaluation of IMERG and ERA5 quantitative precipitation estimates over the Southern Ocean using shipborne observations. *Journal of Applied Meteorology and Climatology*, *62*(11), 1479–1495. https://doi.org/10.1175/JAMC-D-23-0039.1

Montoya Duque, E., Huang, Y., Siems, S. T., May, P. T., Protat, A., & McFarquhar, G. M. (2022). A characterization of clouds and precipitation over the Southern Ocean from synoptic to micro scales during the CAPRICORN field campaigns. *Journal of Geophysical Research: Atmospheres*, *127*(17), e2022JD036796. https://doi.org/10.1029/2022JD036796

Morrison, A. E., Siems, S. T., & Manton, M. J. (2011). A three-year climatology of cloud-top phase over the Southern Ocean and North Pacific. *Journal of Climate*, *24*(9), 2405–2418. https://doi.org/10.1175/2010jcli3842.1

Morrison, H., Curry, J., & Khvorostyanov, V. (2005). A new double-moment microphysics parameterization for application in cloud and climate models. Part I: Description. *Journal of the Atmospheric Sciences*, *62*(6), 1665–1677. https://doi.org/10.1175/jas3446.1

Morrison, H., Thompson, G., & Tatarskii, V. (2009). Impact of cloud microphysics on the development of trailing stratiform precipitation in a simulated squall line: Comparison of one– and two–moment schemes. *Monthly Weather Review*, *137*(3), 991–1007. https://doi.org/10.1175/2008MWR2556.1

Mossop, S. (1970). Concentrations of ice crystals in clouds. *Bulletin of the American Meteorological Society*, *51*(6), 474–479. https://doi.org/10.1175/1520-0477(1970)051<0474:coicic>2.0.co;2

Naud, C. M., Jeyaratnam, J., Booth, J. F., Zhao, M., & Gettelman, A. (2020). Evaluation of modeled precipitation in oceanic extratropical cyclones using imerg. *Journal of Climate*, *33*(1), 95–113. https://doi.org/10.1175/JCLI-D-19-0369.1

Niu, G.-Y., Yang, Z.-L., Mitchell, K. E., Chen, F., Ek, M. B., Barlage, M., et al. (2011). The community Noah land surface model with multi-parameterization options (Noah-MP): 1. Model description and evaluation with local-scale measurements. *Journal of Geophysical Research*, *116*(D12), D12109. https://doi.org/10.1029/2010JD015139

Oue, M., Tatarevic, A., Kollias, P., Wang, D., Yu, K., & Vogelmann, A. M. (2020). The cloud-resolving model radar SIMulator (CR-SIM) version 3.3: Description and applications of a virtual observatory. *Geoscientific Model Development*, *13*(4), 1975–1998. https://doi.org/10.5194/gmd-13-1975-2020

Pan, H.-l., & Wu, W.-S. (1995). Implementing a mass flux convection parameterization package for the NMC medium-range forecast model. *National Oceanic and Atmospheric Administration*.

Pavolonis, M. J. (2010). GOES-R Advanced Baseline Imager (ABI) algorithm theoretical basis document for cloud type and cloud phase, version 2.0. *NOAA NESDIS Center for Satellite Applications and Research Algorithm Theoretical Basis Doc*, 86. Retrieved from https://www.star.nesdis.noaa.gov/goesr/docs/ATBD/Cloud_Phase.pdf

Protat, A., & CSIRO, & Marine National Facility. (2020). RV investigator BOM atmospheric data overview (2016 onwards). v2 [dataset]. CSIRO. Data Collection. https://doi.org/10.25919/5f688fcc97166

Rauber, R. M., Hu, H., Dominguez, F., Nesbitt, S. W., McFarquhar, G. M., Zaremba, T. J., & Finlon, J. A. (2020). Structure of an atmospheric river over Australia and the Southern Ocean. Part I: Tropical and midlatitude water vapor fluxes. *Journal of Geophysical Research: Atmospheres*, *125*(18), e2020JD032513. https://doi.org/10.1029/2020JD032513

Sellegri, K., Peltola, M., Saint-Macary, A., Barthelmeß, T., Rocco, M., Moore, K. A., et al. (2023). Sea2Cloud: From biogenic emission fluxes to cloud properties in the southwest Pacific. *Bulletin of the American Meteorological Society*, *104*(5), E1017–E1043. https://doi.org/10.1175/BAMS-D-21-0063.1

Siems, S. T., Huang, Y., & Manton, M. J. (2022). Southern Ocean precipitation: Toward a process-level understanding. *WIREs Climate Change*, *13*(6), e800. https://doi.org/10.1002/wcc.800

Skamarock, W. C., Klemp, J. B., Dudhia, J., Gill, D. O., Liu, Z., Berner, J., et al. (2019). *A description of the advanced research WRF model version 4. Software* (p. 145). National Center for Atmospheric Research.

Sotiropoulou, G., Sullivan, S., Savre, J., Lloyd, G., Lachlan-Cope, T., Ekman, A. M. L., & Nenes, A. (2020). The impact of secondary ice production on Arctic stratocumulus. *Atmospheric Chemistry and Physics*, *20*(3), 1301–1316. https://doi.org/10.5194/acp-20-1301-2020

Stein, A. F., Draxler, R. R., Rolph, G. D., Stunder, B. J. B., Cohen, M. D., & Ngan, F. (2015). NOAA's HYSPLIT atmospheric transport and dispersion modeling system. *Bulletin of the American Meteorological Society*, *96*(12), 2059–2077. https://doi.org/10.1175/BAMS-D-14-00110.1

Tan, J., Huffman, G. J., Bolvin, D. T., & Nelkin, E. J. (2019). Diurnal cycle ofIMERG V06 precipitation. *Geophysical Research Letters*, *46*(13), 584–592. https://doi.org/10.1029/2019GL085395

Tan, J., Petersen, W. A., Kirstetter, P. E., & Tian, Y. (2017). Performance of IMERG as a function of spatiotemporal scale. *Journal of Hydrometeorology*, *18*(2), 307–319. https://doi.org/10.1175/JHM-D-16-0174.1

Tang, G., Clark, M. P., Papalexiou, S. M., Ma, Z., & Hong, Y. (2020). Have satellite precipitation products improved over last two decades? A comprehensive comparison of GPM IMERG with nine satellite and reanalysis datasets. *Remote Sensing of Environment*, *240*, 111697. https://doi.org/10.1016/j.rse.2020.111697

Tansey, E., Marchand, R., Protat, A., Alexander, S. P., & Ding, S. (2022). Southern Ocean precipitation characteristics observed from CloudSat and ground instrumentation during the Macquarie island cloud & radiation experiment (MICRE): April 2016 to March 2017. *Journal of Geophysical Research: Atmospheres*, *127*(5), e2021JD035370. https://doi.org/10.1029/2021jd035370

Truong, S., Huang, Y., Lang, F., Messmer, M., Simmonds, I., Siems, S., & Manton, M. (2020). A climatology of the marine atmospheric boundary layer over the Southern Ocean from four field campaigns during 2016–2018. *Journal of Geophysical Research: Atmospheres*, *125*(20), e2020JD033214. https://doi.org/10.1029/2020jd033214

Truong, S. C. H. (2023). WRF model namelist for "characteristics and variability of precipitation across different sectors of an extra-tropical cyclone – A case study over the high-latitudes of the Southern Ocean". [Software]. Zenodo. Retrieved from https://zenodo.org/records/10080804

Truong, S. C. H., Huang, Y., Siems, S. T., Manton, M. J., & Lang, F. (2022). Biases in the thermodynamic structure over the Southern Ocean in ERA5 and their radiative implications. *International Journal of Climatology*, *42*(15), 1–18. https://doi.org/10.1002/joc.767218

Turk, F. J., Arkin, P., Ebert, E. E., & Sapiano, M. R. P. (2008). Evaluating high-resolution precipitation products. *Bulletin of the American Meteorological Society*, *89*(12), 1911–1916. https://doi.org/10.1175/2008bams2652.1

Ucar/Ncar, E. O. L. (2018). NCAR/EOL ISS radiosonde data. version 1.0. *EOL Data Archieve*. https://doi.org/10.5065/D69P30HG

Vignon, É., Alexander, S., DeMott, P., Sotiropoulou, G., Gerber, F., Hill, T., et al. (2021). Challenging and improving the simulation of mid-level mixed-phase clouds over the high-latitude Southern Ocean. *Journal of Geophysical Research: Atmospheres*, *126*(7), e2020JD033490. https://doi.org/10.1029/2020jd033490

Wang, Z., Siems, S. T., Belusic, D., Manton, M. J., & Huang, Y. (2015). A climatology of the precipitation over the Southern Ocean as observed at Macquarie island. *Journal of Applied Meteorology and Climatology*, *54*(12), 2321–2337. https://doi.org/10.1175/jamc-d-14-0211.1

Ye, H., Fetzer, E. J., Wong, S., Behrangi, A., Olsen, E. T., Cohen, J., et al. (2014). Impact of increased water vapor on precipitation efficiency over northern Eurasia. *Geophysical Research Letters*, *41*(8), 2941–2947. https://doi.org/10.1002/2014GL059830

Zheng, Y., & Li, Z. (2019). Episodes of warm-air advection causing cloud-surface decoupling during the MARCUS. *Journal of Geophysical Research: Atmospheres*, *124*(22), 12227–12243. https://doi.org/10.1029/2019JD030835

References From the Supporting Information

Delanoë, J., Protat, A., Vinson, J., Brett, W., Caudoux, C., Bertrand, F., et al. (2016). Basta: A 95-GHz FMCW Doppler radar for cloud and fog studies. *Journal of Atmospheric and Oceanic Technology*, *33*(5), 1023–1038. https://doi.org/10.1175/jtech-d-15-0104.1

Louf, V., Protat, A., Warren, R. A., Collis, S. M., Wolff, D. B., Raunyiar, S., et al. (2019). An integrated approach to weather radar calibration and monitoring using ground clutter and satellite comparisons. *Journal of Atmospheric and Oceanic Technology*, *36*(1), 17–39. https://doi.org/10.1175/jtech-d-18-0007.1

Royer, P., Bizard, A., Sauvage, L., & Thobois, L. (2014). Validation protocol and intercomparison campaigns with the R-MAN510 aerosol lidar. *Proceedings of 17th International Symposium for the Advancement of Boundary-Layer Remote Sensing, Auckland, New Zealand, University of Auckland*. https://doi.org/10.13140/2.1.4778.1767